# nature communications



**Article** 

https://doi.org/10.1038/s41467-025-63817-0

# Explicit error coding can mediate gain recalibration in continuous bump attractor networks

Received: 2 April 2024

Accepted: 28 August 2025

Published online: 17 October 2025



Gorkem Secer <sup>1,2,3</sup> □, James J. Knierim <sup>2,3,4,6</sup> & Noah J. Cowan <sup>1,3,5,6</sup> □

Continuous bump attractor networks (CBANs) are a prevailing model for how neural circuits represent continuous variables. CBANs maintain these representations by temporally integrating inputs that encode differential (i.e., incremental) changes to a given variable. The accuracy of this computation hinges on a precisely tuned integration gain. Experiments have shown that the brain can recalibrate this gain using ground-truth sensory information, yet existing CBAN models rely on biologically implausible or currently unknown plasticity rules for recalibration. Here, we demonstrate that ring-type CBANs can recalibrate their integration gain through two mechanisms that rely on well-established, biologically plausible forms of plasticity. In the first mechanism, the spatially distributed synapses conveying incremental information to the attractor are plastic, allowing the integration gain to become transiently inhomogeneous during recalibration. In the second, plasticity is implemented in other components of the network, keeping the gain homogeneous during recalibration. Both mechanisms require explicit error signals that drive plasticity. We instantiate each mechanism within a CBAN, demonstrating their potential for biologically plausible, adaptive coding of continuous variables.

The brain's ability to represent continuous variables, such as location, time, and sensory information, is fundamental to our understanding and interaction with the external world. A compelling theoretical framework for how the brain constructs these representations is provided by continuous bump attractor networks (CBANs) in a diverse range of brain functions, such as orientation tuning in visual cortex<sup>1</sup>, working memory<sup>2,3</sup>, evidence accumulation and decision-making<sup>4-7</sup>, and spatial navigation<sup>8-12</sup>.

The CBAN is a class of recurrent neural network that maintains persistent patterns of population activity through interactions among its neurons. This persistent activity typically forms the shape of a 'bump' when visualized on an appropriate topological arrangement of

neurons (known as a low-dimensional manifold), such as a plane, circle, or torus<sup>13</sup>. Although the shape of the activity bump is constrained by network dynamics, its center location can vary along this low-dimensional manifold, corresponding to different values of the encoded continuous variable. Neural activity consistent with these key properties of CBANs, namely, the activity bump and the low-dimensional manifold, have been observed in recordings from various regions of the mammalian brain that encode continuous variables<sup>14–16</sup>. More conclusive and direct evidence for CBANs has been found in the central complex of the fly brain, where a biological CBAN encoding the fly's heading angle, a continuous variable, has been identified based on the connectome and a combination of calcium

<sup>1</sup>Laboratory for Computational Sensing and Robotics, Johns Hopkins University, Baltimore, MD, USA. <sup>2</sup>Zanvyl Krieger Mind/Brain Institute, Johns Hopkins University, Baltimore, MD, USA. <sup>3</sup>Kavli Neuroscience Discovery Institute, Johns Hopkins University School of Medicine, Baltimore, MD, USA. <sup>4</sup>Solomon H. Snyder Department of Neuroscience, Johns Hopkins University School of Medicine, Baltimore, MD, USA. <sup>5</sup>Department of Mechanical Engineering, Johns Hopkins University, Baltimore, MD, USA. <sup>6</sup>These authors jointly supervised this work: James J. Knierim, Noah J. Cowan. ⊠e-mail: gsecer1@jhu.edu; ncowan@jhu.edu

imaging and optogenetics<sup>17–20</sup>. While these experimental findings support the idea of brain circuits employing CBANs to represent continuous variables, the neural mechanisms that enable CBANs to accurately update their representations in response to changes in continuous variables remain incompletely understood.

CBANs update their representations of a continuous variable based on two distinct types of inputs. The first type provides 'absolute' information, namely, the true value of a continuous variable, such as spatial location relative to visual landmarks or the item to be held in working memory. When this absolute information is available, it provides input to a specific location on the CBAN's low-dimensional manifold that is associated with the true value of the continuous variable. In response to this localized input, the internal dynamics of the CBAN create a basin of attraction on its low-dimensional manifold toward which the activity bump gravitates, bringing the representation into close alignment with the actual value of the continuous variable<sup>21-23</sup>. This theoretical phenomenon has been experimentally observed in the biological CBAN within the fly central complex<sup>17</sup> and, more indirectly, in the spatially tuned neurons of the hippocampus and entorhinal cortex-two regions modeled as CBANs in the mammalian brain<sup>24-28</sup>.

In contrast to the first type of inputs providing absolute information to the CBAN, the second type provides 'differential' information, namely, the changes in the continuous variable. Sources of such inputs may be, for instance, self-generated movements providing velocity information in the context of spatial navigation or sensory cues serving as pieces of evidence in the context of decision-making. In response to these inputs, the internal dynamics of the CBAN shift the activity bump along its low-dimensional manifold—in a process akin to mathematical integration—such that the bump's location reflects the value of the continuous variable. However, the encoding accuracy of this integration process depends critically on an additional factor, namely, the integration gain of the network that relates the cumulative change in the continuous variable to the updating of the bump location in a proportional manner<sup>29,30</sup>. If this gain factor is miscalibrated. the result of the CBAN's integration process begins drifting away from the true value of the continuous variable; simply stated, it accumulates error. In the presence of absolute information sources such as visual landmarks in the context of spatial navigation, the aforementioned 'basin' mechanism corrects errors, preventing them from accumulating. However, without absolute information, error accumulation continues due to the miscalibrated integration gain. The error accumulation may eventually cause, for example, a CBAN that integrates evidence to reach a decision threshold (associated with activation of a specific neuron above a certain level<sup>4</sup>) either too soon or too late. Likewise, a miscalibrated CBAN integrating an animal's angular head velocity may overestimate or underestimate the correct head direction. Thus, a finely tuned integration gain is crucial for a CBAN to accurately encode a continuous variable based on inputs with only differential information.

Recent data from time cells and place cells of the rodent hippocampal formation, hypothesized to rely on CBANs<sup>31</sup>, showed that the brain's integration gain is indeed a plastic variable whose value is adjusted based on the feedback from absolute information sources<sup>32,33</sup>. In the first study that demonstrated this phenomenon on place cells<sup>33</sup>, the virtual visual landmarks, which provided the absolute information, were moved as a function of the animal's movement on a circular track. This manipulation induced persistent errors between the encoded location, derived from angular path integration, and the actual location relative to the moving landmarks. Consequently, the brain recalibrated its integration gain, adjusting it in both direction and magnitude to reduce the positional encoding error. The recalibration was most evident after the landmarks were extinguished: The space encoded by place cells during pure path integration either expanded or contracted, depending on the direction of the preceding landmark

manipulation. Present CBAN models treat the integration gain either as a constant set via carefully chosen, hard-wired model parameters (e.g., synaptic weights)<sup>11,12,34-36</sup> or as a variable learned via plasticity rules that are not biologically plausible<sup>37</sup> or are unproven<sup>38</sup>. Although these models showed the possibility of gain tuning, fundamental insights into the error-based neural mechanisms underlying this tuning are missing. Therefore, given the biological relevance and theoretical importance of this recalibration phenomenon, an open question remains: What are the critical factors enabling a CBAN to recalibrate its integration gain based on feedback from absolute information sources?

In the present paper, we aim to address this question and generate testable physiological predictions about the neural mechanisms underlying gain recalibration in brain circuits that encode continuous variables. As a representative problem, we focus on hippocampal place coding and theoretically investigate how visual landmarks-an absolute information source-might recalibrate the integration gain of a CBAN encoding an animal's position on a circular track<sup>33</sup>. We identify two distinct gain recalibration mechanisms within a ring attractor. The first mechanism involves Hebbian plasticity in the synaptic connections between the differential inputs and the attractor, allowing the integration gain to become spatially inhomogeneous during recalibration. This inhomogeneity can be transient, fading away as the system continually uses the feedback from absolute information sources for recalibration. In contrast, the second mechanism features nonplastic differential-input synapses and maintains spatially homogeneous integration gain during recalibration, with path-integration gain plasticity arising through nonsynaptic mechanisms. Importantly, we provide strong theoretical evidence that in CBAN models, both recalibration mechanisms depend on explicit error signals at the neuronal level, unlike error correction that can occur automatically without explicit error signaling (Fig. 1A). Our findings predicts a previously untested functional role for the absolute information sources within the putative CBAN circuits of the brain and highlight a critical modification to prior CBAN models, which lack an explicit error signal. Finally, we propose modified CBAN models incorporating explicit error signals to recalibrate their integration gains. Our approach and the organization of the paper can be found in Fig. 1B.

#### Results

# Model setup: ring attractor network

A CBAN is a recurrently connected neural network where neighboring neurons excite one another and inhibit distant neurons according to a connectivity pattern known as local excitation and global inhibition<sup>1,39</sup>. This connectivity gives rise to a persistent bump of activity as a stable equilibrium state of the system. For large networks (i.e., in the limit as the number of neurons goes to infinity; but see<sup>40</sup>) where this connectivity pattern remains consistent across the network, the equilibrium states form a continuum, known as attractor states<sup>39,41-43</sup>. The arrangement of neurons and the exact pattern of the recurrent connectivity determine the topology of this attractor. In the case of a ring attractor, neurons are arranged as a topological ring<sup>11</sup>. By sustaining an activity bump whose location can be shifted around the ring based on external inputs (i.e., the differential and absolute information sources), a ring attractor network is well-suited to represent a variable on a closed curve (e.g., the angular location of an animal on a onedimensional (1D) circular track). Because integration-gain recalibration has been demonstrated in place cells of rats running on a circular track, we choose to model this process with a ring attractor, a computationally tractable framework naturally suited for encoding circular variables.

Various architectures have been proposed for ring attractors<sup>8,10-12</sup>. From this set of possible architectures, we restrict our analysis to the three-ring architecture because of its consistency with the anatomy of the fly central complex<sup>18,19</sup> and its generalizability to higher

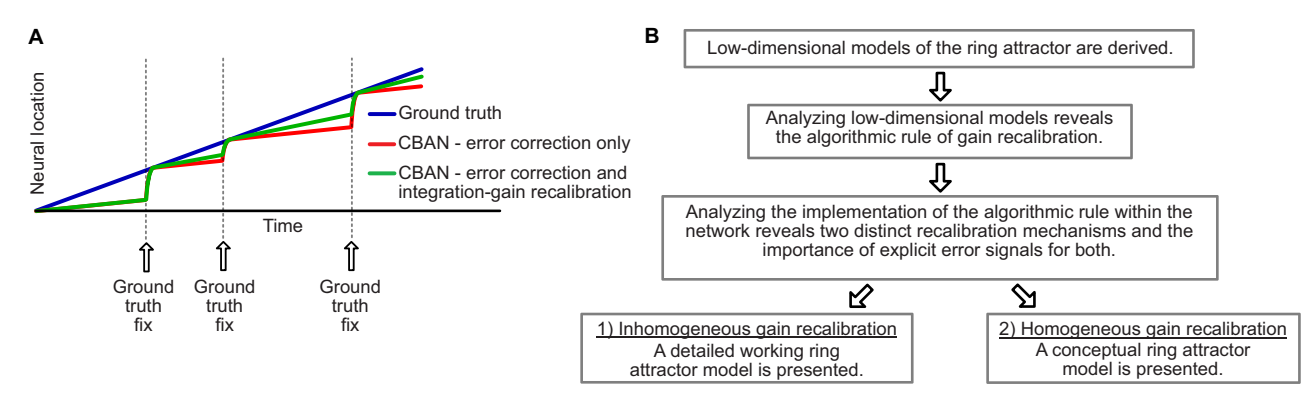


**Fig. 1** | **Conceptual overview and methodological roadmap. A** Conceptual illustration of the main question addressed in the present paper: If a CBAN (Continuous Bump Attractor Network) has an inaccurate integration gain, its representation of a continuous variable accumulates errors. A classical finding from decades of CBAN research is that these representational errors are automatically corrected by ground truth signals—a process known as the "ground truth fix" without requiring an *explicit code of the error* at the level of single neurons. This raises the question of whether a CBAN can automatically learn from these errors and recalibrate its integration gain without an explicit error code. In this paper, we

present theoretical evidence that an explicit error signal, in the form of a rate code, plays a crucial role in the recalibration of the CBAN's integration gain. Because classical CBANs without an explicit error code lack the ability to recalibrate their integration gain, their representational errors continue to accumulate at the same rate until the ground truth signals become available, at which point they are corrected (red line). In contrast, a CBAN equipped with an explicit error code does not only correct representational errors but also recalibrates its integration gain, gradually reducing the rate at which errors accumulate over time (green line). B Our technical approach and how it is organized across the paper.

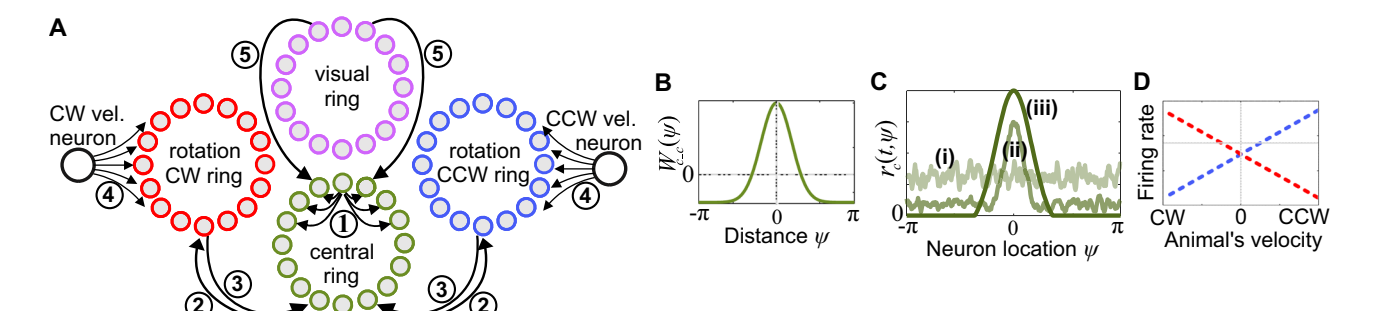


**Fig. 2** | **Ring attractor network model** <sup>10,36,44,93</sup>. **A** Schematic representation of the model. The central ring forms the main body of the model based on its recurrent connections (labeled with o). Its reciprocal offset connections with the rotation CW and CCW rings (labeled with o and o) create a push-pull mechanism that modulates the intrinsically controlled neural activity of the central ring based on external inputs from the CW and CCW velocity neurons (labeled with o). An additional external input is provided to the central ring from the visual ring (labeled with o), corresponding to a set of sensory neurons that are tuned to visual landmarks. **B** Synaptic weight function  $W_{c-c}: S^1 \to \mathbb{R}$  that describes the recurrent

connections within the central ring according to the well-known local excitation and global inhibition pattern. **C** Numerical demonstration of how recurrent connectivity within the central ring can autonomously maintain a persistent activity bump. Simulation of the central ring neurons was started with initial conditions that were assigned pseudo-randomly (light green line labeled with (i)). Within 100 milliseconds, a bump of activity emerges (medium green line labeled with (ii)). Eventually, the firing rates converge to an equilibrium, forming a persistent bump of activity (dark green line labeled with (iii)). **D** Tuning curves of CCW and CW velocity neurons are shown with blue-dashed and red-dashed lines, respectively.

dimensions<sup>36,44</sup>. For example, augmenting the 1D ring-arrangement of neurons in this architecture to a 2D toroid naturally leads to an attractor that is well-suited to represent two continuous variables<sup>13</sup>, as in grid and place cells<sup>36,44</sup>. As the name suggests, the three-ring attractor consists of three groups of neurons, each ordered in a ring arrangement: a central ring, a clockwise (CW) rotation ring, and a counter-clockwise (CCW) rotation ring<sup>8,11</sup>. Neurons within these three rings are interconnected via intrinsic connections. Additionally, they receive inputs via extrinsic connections from upstream neurons that encode the velocity information (i.e., a 'differential' type of input) and from a fourth ring that encodes the positional feedback from visual landmarks (i.e., an 'absolute' type of input) (Fig. 2A).

Our ultimate goal is to garner insights into how the three-ring attractor network's integration gain—hereafter referred to as the path-integration (PI) gain—can be recalibrated by visual landmarks. Intuitively, the PI gain determines how much the activity bump shifts around the central ring for a given amount of the animal's movement in physical space. To attain our goal, we will first reduce the complex

network dynamics into a simplified, 1D differential equation<sup>39</sup>. Prior work derived such models for networks wherein the synaptic weights are constrained to be spatially uniform and static<sup>45,46</sup>. Here, we relax some of these constraints and develop a simplified model of the ring attractor network, progressively, starting from the central ring (Section "Control theory reveals algorithmic conditions for PI-gain recalibration"). We next include rotation rings to model the response of the network dynamics to self-movement inputs, which reveals an analytical expression of PI gain and its spatially distributed structure (Section "The need for an explicit error code to meet the algorithmic conditions for PI-gain recalibration"). Finally, we extend the simplified model to include the positional feedback from visual landmarks, where we observe how the strength of this feedback may be modulated by changes in the PI gain during recalibration (Section "The visual ring provides gain-dependent positional feedback that corrects path integration"). This simplified model allows us to rigorously identify algorithmic conditions (Section "Control theory reveals algorithmic conditions for PI-gain recalibration") for PI-gain recalibration, from

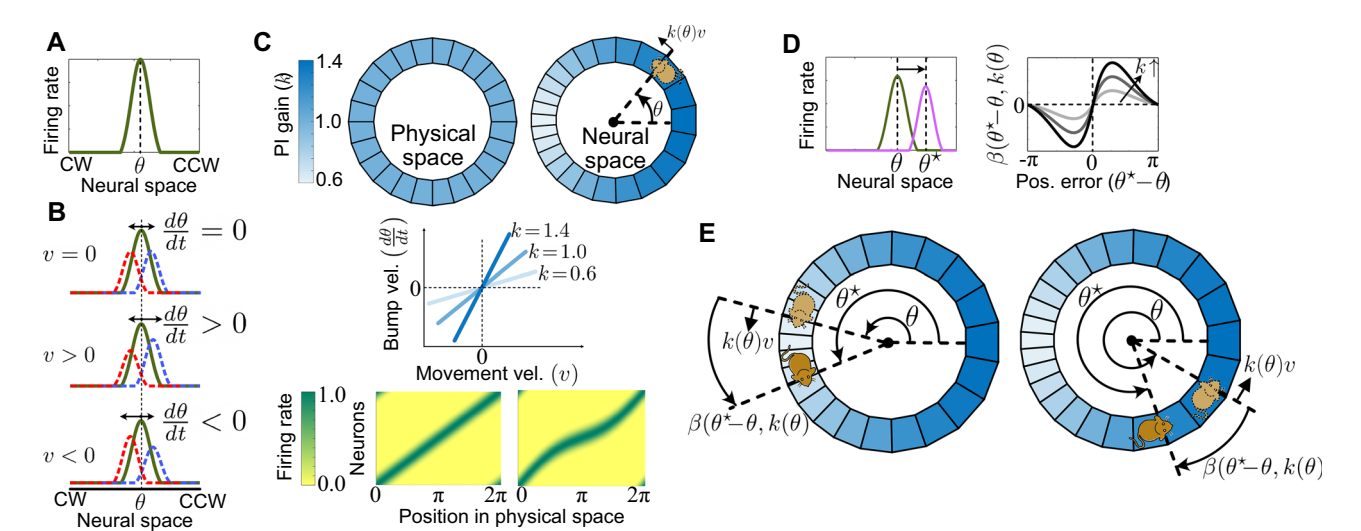


**Fig. 3** | **Models of the ring attractor's position representation.** A The representation  $\theta$ , decoded from the peak location of an ansatz solution  $\hat{r}_c$ . **B** Implementation of angular PI based on the push-pull mechanism formed by reciprocal connections between the central (green) and rotation rings (CCW: blue, CW: red). The top row shows the balanced inputs from these rotation rings about the central ring's current activity-bump location  $\theta$  when the animal is stationary (v = 0). The middle and bottom rows show the imbalance in these synaptic inputs in the direction of the animal's movement (middle: v > 0; bottom v < 0), which in turn shifts the activity bump in the same direction. **C** Cartoon illustration of neural dynamics given in Eq. (3). Top left: Circular track. Top right: Internal representation of this track with a spatially inhomogeneous PI gain  $k(\theta)$  ranging from 0.6 at  $\theta = \pi$  to 1.4 at  $\theta = 0$ . The bump location  $\theta$  corresponding to the network's position representation is visualized by the pale brown rat. As the rat moves through physical space with velocity v, the representation moves through neural space according to  $k(\theta)v$ . Middle: The relationship between the bump velocity  $\frac{d\theta}{dt}$  and the animal's

velocity v. Bottom left: Firing rate map of uniformly distributed cells in a `traditional' network model with a global PI gain  $k(\theta) = 1$ . Bottom right: The same rate map for a network model with spatially inhomogeneous PI gain  $k(\theta)$ . **D** Left shows the central ring's activity bump (green) and the bump-shaped synaptic input onto the central ring from the visual ring (pink). Right shows the model  $\beta$  of the stabilizing visual feedback emerging from the interaction between these two bumps as a function of the *error*—namely, the discrepancy  $\theta^* - \theta$ . As indicated by the opacity of the lines, this feedback may depend on the value of the PI gain. **E** Cartoon illustration of neural dynamics given in Eq. (5). The pale brown rat symbolizes the internal representation  $\theta$  as in C, whereas the medium brown rat symbolizes the actual location  $\theta^*$  as represented by the visual drive. The temporal change in  $\theta$  is controlled by the PI term  $k(\theta)v$  and the visual feedback term  $\beta(\theta^* - \theta, k_0)$  as visualized by two arrows acting on the pale brown rat. Left shows a case where the PI has a low gain  $k(\theta) < 1$ , thus underestimating the position relative to the landmarks. Right shows the overestimation case due to "high" PI gain.

which we derive the mechanistic requirements for a network to implement the recalibration (Section "The need for an explicit error code to meet the algorithmic conditions for PI-gain recalibration").

**Ansatz solution to central-ring dynamics.** Parameterizing a neuron based on its angle  $\psi \in S^1$  in the circular neural space, we can express the dynamics of the central ring as follows:

$$\tau_{\rm c} \frac{\partial r_{\rm c}(t, \psi)}{\partial t} = -r_{\rm c}(t, \psi) + \sigma \left[ W_{\rm c-c}(\psi) \otimes r_{\rm c}(t, \psi) + I_{\rm ext}(t, \psi) \right]. \tag{1}$$

Here,  $r_{\rm c}(t,\psi)$  denotes the firing rate of the central ring neuron  $\psi$  at time t,  $\tau_{\rm c}$  denotes the synaptic time constant of central ring neurons,  $\circledast$  denotes the circular convolution operation,  $\sigma$  denotes an activation function (chosen as a rectified linear unit) in our current study),  $I_{\rm ext}(t,\psi)$  denotes external synaptic inputs to the central ring, and  $W_{\rm c-c}:S^1\to\mathbb{R}$  denotes a rotationally invariant synaptic weight function that describes the recurrent connections ( $\odot$  in Fig. 2A) (Fig. 2B). At the limit, as the network size increases  $^{39,41,42}$ , the recurrent connectivity leads to stabilization of a persistent "bump" of neural activity, a hallmark of the CBANs.

The activity bump is constrained by the network dynamics to take nonzero values in a limited range (i.e., compact support) and to have a symmetric shape with a single peak  $\theta$  (i.e., even symmetry about the peak) (Fig. 2C). This peak location, which corresponds to the internal representation of the animal's position, can vary along the central ring in response to external synaptic inputs  $I_{\rm ext}$ . Even though we are unable to obtain an exact analytical solution to the central-ring dynamics in Eq. (1) to fully describe this dynamic response, we can 'guess' a solution form that can describe its general properties without relying on a

specific function as follows:

$$r_c(t, \psi) = \hat{r}_c(\psi - \theta(t)). \tag{2}$$

Here,  $\hat{r}_c(\psi - \theta(t))$  denotes a function, such as a thresholded Gaussian or a sinusoid 11,21,47-50, describing the persistent activity bump with the previously mentioned symmetry and width properties (see Supplementary Note 3 for further details), and  $\psi = \theta(t)$  denotes the bump location associated with its peak (Fig. 3A). The guess we make with the function  $\hat{r}_c$  is termed an *ansatz* solution. Assuming that the activity bump's symmetric shape and compactly supported width remain fixed, the ansatz solution enables us to derive a 1D differential equation that governs the dynamics of the bump location  $\theta$  in response to external inputs  $I_{\rm ext}$ . The external inputs are provided by neurons of the rotation rings and the visual ring (see Supplementary Note 1 for an analytical expression of these inputs). We progressively incorporate these parts into our model in the following subsections.

Rotation rings provide inputs for angular path integration via a spatially distributed gain. We begin with the rotation rings that combine positional information and self-movement velocity information based on inputs from two afferent sources: (i) The central ring provides the positional information, represented by its bump location, to both rotation rings through the synaptic weight functions  $W_{c-cw}$ ,  $W_{c-ccw}$ :  $S^1 \to \mathbb{R}$  (② in Fig. 2A). (ii) Velocity-dependent differential firing of CW and CCW 'velocity' neurons, namely,  $u_{cw} = u^0 - \alpha_{cw} v$  and  $u_{ccw} = u^0 + \alpha_{ccw} v$  (Fig. 2D), signal the animal's velocity v to the respective rotation rings through synaptic weights  $W_{v-cw}$ ,  $W_{v-ccw}$ :  $S^1 \to \mathbb{R}$  (④ in Fig. 2A). Combining these inputs, we obtain ansatz solutions  $\hat{r}_{cw}$ ,  $\hat{r}_{ccw}$  to the CW and CCW rotation rings' firing rates under

the assumption that the synaptic dynamics of rotation rings are sufficiently fast as described in Supplementary Note 3. These solutions describe an activity bump within the rotation rings, derived from the ansatz  $\hat{r}_c$  for the central ring.

The rotation rings project reciprocally back to the central ring via offset connections, where a CW/CCW rotation-ring neuron at a specific location in the angular neural space connects to a central ring neuron at a slightly offset location in the same direction (3 in Fig. 2A), giving rise to a feedback push-pull structure. How does this connectivity structure respond to external inputs from the velocity neurons? If we assume that the CW and CCW components are symmetric in both the synaptic weights of the push-pull connectivity and the baseline firing rates of the velocity neurons (a commonly made assumption), then the rotation rings fire equally when the animal is immobile (i.e., v = 0). As a result, they provide balanced inputs to the central ring, keeping the bump location  $\theta$  unchanged ( $\frac{d\theta}{dt}$  = 0). In contrast, inputs from the CW and CCW velocity neurons modulate the activity of the respective rotation rings differentially when the animal is moving  $(v \neq 0)$ . This modulation causes the input from the rotation rings to become imbalanced about the central ring's current activity bump. In response to this imbalance, the central ring shifts its activity bump at a rate proportional to the animal's velocity (Fig. 3B). This process is known as angular path integration; hereafter, we refer to it simply as path integration (PI).

Under the classical assumptions (e.g., the movement causes a weak differential change in the inputs to the central ring), the ansatz solutions,  $\hat{r}_{c}$ ,  $\hat{r}_{cw}$ ,  $\hat{r}_{cw}$  can be used to derive a simplified model for the PI process—specifically, a 1D differential equation governing the temporal evolution of the position representation  $\theta$ . Applying the dimensionality reduction protocol detailed between Supplementary Notes 2 to 3.2, this model takes the following form:

$$\frac{d\theta}{dt} = k(\theta)v. \tag{3}$$

This equation shows that the PI process updates the bump location  $\theta$  in proportion to the animal's velocity v with a gain factor  $k(\theta)$ . This factor simply represents the ring attractor network's PI gain, and its analytical expression takes the following form:

$$k(\theta) = \frac{-b}{\tau_{c} \left\| \frac{\partial \hat{r}_{c}}{\partial \psi} \right\|^{2}} \int_{0}^{2\pi} \frac{\partial^{2} \hat{r}_{c}(\psi - \theta)}{\partial \psi^{2}} \sum_{i \in \{\text{cw, ccw}\}} \alpha_{i} W_{i-c}(\psi) W_{v-i}(\psi) \operatorname{sign}[\hat{r}_{i}(\psi, \theta, 0)] d\psi.$$

$$(4)$$

Here, *i* denotes the index of the summation, representing either the CW or CCW rotation ring,  $\alpha$  denotes the absolute value of the slope of the velocity neurons' tuning curves, b denotes the value of the offset in the connections between rotation rings and the central ring, and | | · | denotes the magnitude (i.e., root-mean-square) of an expression. Intuitively, this equation shows that the PI gain emerges from the interaction between external velocity inputs and the attractor's recurrent dynamics, which together process and transform the animal's movement into the bump's movement. In this interaction, if the synaptic processes operate more quickly (lower time constant  $\tau_c$ ), the network responds more rapidly to the velocity inputs, resulting in an increased PI gain. Similarly, larger synaptic weights in  $W_{i-c}$  (corresponding to rotation-to-central ring synapses) or in  $W_{v-i}$  (corresponding to velocity-to-rotation ring synapses), or steeper velocity-neuron slopes  $\alpha$  enhance the velocity input onto the central ring, accelerating the bump movement, thereby increasing the PI gain. The attractor's bump magnitude, however, has the opposite effect. A larger bump magnitude resists movement, requiring stronger inputs, hence resulting in a reduced PI gain. A detailed account of how every parameter in Eq. (4) influences the PI gain will be given in Section "The need for an explicit error code to meet the algorithmic conditions for PI-gain recalibration", where we explore how temporal changes in network parameters can recalibrate the PI gain over time.

Beyond showing how network parameters relate to the value of PI gain, our derivation of Eq. (4) uncovers a previously unknown property of the PI gain within a ring attractor model: The PI gain is locally distributed across the network, as governed by the spatially distributed synaptic weights in the pathway from the velocity neurons onto the central ring (2 and 4 in Fig. 2A). When these weights are spatially uniform (i.e., having the same profile and magnitude), as has always been assumed in previous work<sup>11,36,45,46</sup>, the PI gain is independent of the bump location, resulting in an ideal model with a single, global PI gain under all conditions. If the synaptic weights ever become heterogeneous (a possibility we revisit later), however, this ideal state is no longer maintained; instead, path integration occurs with a PI gain k that varies as a function of the bump location  $\theta$  (Fig. 3C). One may wonder why we even care about this seemingly strange possibility. As will be evident later, for a subset of biologically plausible gain recalibration mechanisms (e.g., tuning the distributed synaptic weights from the velocity neurons to the rotation rings), such inhomogeneities in the PI gain are inevitable—though they may diminish with repeated use of feedback from landmarks. By contrast, for other mechanisms (e.g., tuning the slope  $\alpha$  of the velocity inputs), the system can always maintain a single, global PI gain. Nevertheless, our derivation of Eq. (4) applies to both cases and forms the foundation of our analytical investigation of the PI-gain recalibration.

The visual ring provides gain-dependent positional feedback that corrects path integration. Next, we include in our simplified model the influence of external inputs from the visual ring (Fig. 2A). The visual ring receives no explicit inputs; instead, its neurons are presumed to autonomously fire at specific locations of the animal relative to landmarks, capturing the absolute positional information received from visual landmarks available at each position (modeling how egocentric visual processes can calculate position from landmarks is beyond the scope of this paper). Through the synaptic weight function  $W_{\text{vis-c}}: S^1 \to \mathbb{R}$  (⑤, in Fig. 2A), this firing of the visual ring provides the central ring with a bump-like synaptic input encoding the animal's "true" position  $\theta^*$  relative to landmarks<sup>51,52</sup>.

In the ring attractor model, the network's position representation  $\theta$  is anchored to this bump-like synaptic input that encodes the positional feedback  $\theta^*$  from landmarks, as observed in numerous experimental studies on head direction and place cells<sup>24–27</sup>. To determine a simplified, approximate model for how  $\theta$  varies under this anchoring effect, we again apply the dimensionality reduction. Assuming that the visual ring provides a weak and narrow bump-like input, this application leads to the differential equation

$$\frac{d\theta}{dt} = \beta(\theta^* - \theta, k(\theta)) + k(\theta)v, \tag{5}$$

where  $k(\theta)v$  denotes the PI inputs as in the previous section and  $\beta$ :  $S^1 \times \mathbb{R} \to \mathbb{R}$  is a function modeling the influence of visual inputs on  $\theta$ . See Supplementary Note 3.3 for details and the assumptions.

One might think that the influence of the visual ring would depend exclusively on the mismatch between the ring attractor bump and the visual ring bump. However, according to our derivation, the visual input,  $\beta$ , influences the system through two mechanisms: a direct effect, which depends on the discrepancy  $\theta^* - \theta$ , and an indirect effect, mediated through the PI gain  $k(\theta)$ . The direct effect aligns the sign of  $\beta$  with the discrepancy  $\theta^* - \theta$ , forming a negative feedback loop that pulls  $\theta$  toward  $\theta^*$  (Fig. 3D). Indeed, this mechanism alone is sufficient to explain landmark correction in traditional ring attractor models, where the PI gain is fixed due to static network parameters. In a ring attractor

model capable of recalibrating its PI gain, however, the direct effect alone can be insufficient because some network parameters that may be updated to recalibrate the PI gain  $k(\theta)$  may also modulate the landmark correction  $\beta$ , altering its ability to correct discrepancies  $\theta^{\star} - \theta$  (these parameters are explored in Section "The need for an explicit error code to meet the algorithmic conditions for PI-gain recalibration" below). To account for this dual impact, the simplified model in Eq. (5) incorporates dependence of  $\beta$  on the indirect effect  $k(\theta)$ . That is, the model can capture dynamic changes in the landmark correction when there is a change in a network parameter associated with a change in the PI gain. When present, this indirect effect based on the PI gain  $k(\theta)$  modulates only the amplitude of  $\beta$  without altering its sign (different lines in Fig. 3D). See Supplementary Note 3.3 for details and an alternative form of the  $\beta$ .

Together, these direct and indirect effects model the  $\beta$  function and how it anchors the attractor's representation  $\theta$  to the "true" value  $\theta^*$  measured relative to landmarks. When the animal is stationary (i.e., v=0), the direct feedback provided by  $\beta$  ensures  $\theta \to \theta^*$ . During the animal's movement, however, the PI-related term,  $k(\theta)v$  updates  $\theta$  based on the animal's velocity, while  $\beta$  continues to anchor  $\theta$  toward  $\theta^*$ . A well-balanced combination of these terms anchors  $\theta$  around  $\theta^*$  (Fig. 3E). Therefore, Eq. (5) provides a simplified framework that captures the combined influence of PI and visual feedback on the ring attractor network's position representation, forming the basis for our subsequent analysis of the algorithmic and mechanistic conditions necessary for successful PI-gain recalibration.

# Algorithmic and mechanistic requirements for PI-gain recalibration

Experiments showed that the PI gain of the rodent hippocampal system is a plastic variable that can be recalibrated by visual landmarks<sup>33</sup>. In Section "Control theory reveals algorithmic conditions for PI-gain recalibration" below, we leverage the analytical tractability of Eq. (5), a simplified model of the ring attractor network, to identify the algorithmic conditions required for recalibration of its PI gain. Then, in the subsequent Section "The need for an explicit error code to meet the algorithmic conditions for PI-gain recalibration", we use Eq. (4), the analytical expression of the ring attractor's PI gain, to map these algorithmic conditions from the simplified model back to the high-dimensional network dynamics as mechanistic prerequisites for implementing PI-gain recalibration.

Control theory reveals algorithmic conditions for PI-gain recali**bration**. To understand the computations required at an algorithmic level for PI-gain recalibration within a ring attractor network, we first revisit the experimental conditions that led to this recalibration phenomenon<sup>33</sup>; In those experiments, an animal moved on a circular track while an array of visual landmarks was rotated around the track as a function of the animal's velocity and an experimentally controlled, visual gain factor,  $k^*$ . When  $k^* < 1$ , the landmarks moved in the same direction as the animal, decreasing the perceived speed; when  $k^* > 1$ , the landmarks moved in the opposite direction as the animal, increasing the perceived speed; when  $k^* = 1$  (veridical condition), the landmarks remained stationary. To model these experimental conditions in a ring attractor network, we assume that the visual drive, represented by its bump location  $\theta^*$ , moves through the circular neural space at a rate equal to the animal's velocity v times the visual gain  $k^*$ , namely,  $\frac{d\theta^*}{dt} = k^* v$ . The experiments in ref. 33 showed that prolonged exposure to these visual conditions recalibrated the animal's PI gain, resulting in a strong correlation between the average value of the PI gain measured over many laps after the landmarks were removed and the final value of the visual gain  $k^*$  before the landmark removal. What does this result imply in the context of a ring attractor model where the PI gain k is a spatially distributed network parameter? Because the experiments measured the recalibrated PI gain from neural activity

over many laps, the results suggest that the ring attractor network must adjust its PI gain such that the PI gain's *spatial averagek*  $_0 \triangleq \frac{1}{2L} \int_0^{2\pi} k(\theta) d\theta$  converges to the visual gain  $k^*$ , namely,  $\lim_{t \to \infty} k_0(t) = k^*$ . We refer to this exact convergence as *complete recalibration*. At this stage, the mechanistic details of how recalibration can occur remain unclear—specifically, whether the ring attractor adjusts its PI gain uniformly across the neural space, maintaining the same value everywhere, or whether some degree of spatial inhomogeneity emerges spontaneously during the recalibration process. By focusing on the PI gain's spatial average  $k_0$ , nevertheless, we ensure that our subsequent analysis remains robust to such mechanistic differences, as long as any potential spatial fluctuations in the PI gain, defined as  $k_{\rm ac}(\theta) \triangleq k(\theta) - k_0$ , remain within a reasonable range, an assumption that will be further clarified in the following paragraphs.

We proceed by posing a question: What variables in the ring attractor network are important for updating  $k_0$ ? We searched for a general equation that can model these updates based on neural activity levels within the network and the current value of the synaptic weights, assuming an environment with spatially homogenous feedback from visual landmarks (See Supplementary Note 4.1 for further details and assumptions). This search led to a surprisingly simple equation

$$\frac{dk_0}{dt} = g_0(k_0, \theta^* - \theta, v), \tag{6}$$

where  $g_0: \mathbb{R} \times S^1 \times \mathbb{R} \to \mathbb{R}$  denotes a function that instantiates the instantaneous change in  $k_0$  based on three variables: the current gain  $k_0$ , the animal's velocity v and the difference between the visual drive's position representation  $\theta^*$  and the ring attractor's position representation  $\theta$ . By contrast, the update does not directly depend on the specific values of  $\theta$  or  $\theta^*$  because of the assumed spatially uniform visual feedback across the environment. Although there are infinitely many  $g_0$  functions of the form in Eq. (6), some of them may fail to result in Pl-gain recalibration, i.e.,  $k_0$  not converging to the visual gain  $k^*$ . We thus ask what are the necessary and sufficient properties of the Pl-gain update rule  $g_0$  for  $k_0 \to k^*$  (i.e., the fundamental features shared by all successful update rules)?

To seek these fundamental properties, we revisit Eq. (5) along with the positional feedback  $\frac{d\theta^*}{dt} = k^* v$  from landmarks and with the fact that the PI gain's spatial average  $k_0$  varies according to Eq. (6). Perfect convergence of  $k_0$  to  $k^*$  through this update rule would imply that the error between these two gains, namely  $\tilde{k} \triangleq k^* - k_0$ , approaches zero. We refer to this error  $\tilde{k}$  in the PI gain's average component as the gain error.

When the gain error  $\tilde{k}$  is not zero, the influence of path integration on the attractor's position representation  $\theta$  causes some positional error  $\theta \triangleq \theta^* - \theta$  relative to the visual drive  $\theta^*$ . If the gain error were reduced, this positional error would also be reduced, aligning the attractor's representation more closely with the visual drive. This coupling between the gain and positional errors-namely  $\tilde{k}$  and  $\tilde{\theta}$ -prompts us to analyze their temporal progression to garner insights into PI-gain recalibration. To this end, we consider a constant visual gain (as was the case during the first and last epochs of the experiments in ref. 33, when landmarks were present). We then analyze the local stability of the errors k and  $\theta$ , assuming that fluctuations in  $k_{\rm ac}$  decrease following the gain error k, while also making assumptions on the properties of  $g_0$ 's derivatives. This analysis identifies the algorithmic conditions for complete recalibration, where  $k_0$  converges exactly to  $k^*$ , as follows:

#### Formal results

- 1. The animal cannot be stationary, otherwise complete recalibration  $(k_0 \rightarrow k^*)$  is not possible.
- 2. Assuming that the animal remains in motion  $(v \neq 0)$ , we found that complete recalibration requires the PI-gain update rule  $g_0$  to share

the same sign as the product of the animal's velocity v and the ring attractor's positional error  $\tilde{\theta}$  in some neighborhood of  $\tilde{\theta}$  = 0:

$$\operatorname{sign}[g_0(k_0, \tilde{\theta}, \nu)] = \operatorname{sign}[\tilde{\theta} \nu]. \tag{7}$$

3. Assuming that the animal's speed is constant and  $|k_{ac}| \approx 0$ , we additionally found that the system is guaranteed to achieve complete recalibration if this sign condition is satisfied.

The proofs of these formal results along with the specific assumptions made are provided in Supplementary Note 4.2. The first result states a trivial necessary condition: if the animal is stationary. visual landmarks will fully correct positional error  $\tilde{\theta}$ , making gain errors  $\tilde{k}$  imperceptible. The second and third results establish the sign condition in Eq. (7) as both necessary and sufficient. Simply stated, recalibrating the PI gain of a ring attractor is equivalent to increasing it when positional error and velocity align, and decreasing it when they oppose each other. To understand the intuition behind this condition, imagine walking along a circular track with a slightly miscalibrated PI gain  $k_0$ . Suppose your PI gain is *under-calibrated* ( $k_0 < k^* = 1$ ), meaning that you consistently underestimate how far you have traveled. In this case, if you walk CCW (v > 0), your internal position estimate  $\theta$  lags behind your true position  $\theta^*$  in the CCW direction, resulting in a growing positive positional error  $(\tilde{\theta} > 0)$ . Conversely, if you walk CW ( $\nu$  < 0), the same underestimation instead causes  $\theta$  to lag behind in the CW direction, leading to a negative positional error  $(\tilde{\theta} < 0)$ . The crucial point is that in both movement directions, the product  $\tilde{\theta}v$  remains consistently *positive* because the sign of both  $\tilde{\theta}$  and v flip together with movement direction. Likewise, if the PI gain is *over-calibrated* ( $k_0 > k^*$ ), the same reasoning shows that the product  $\tilde{\theta}v$  remains *negative* regardless of movement direction (CCW or CW). Thus, the sign of  $\tilde{\theta}v$ precisely indicates whether the PI gain should be increased or decreased, and Eq. (7) simply formalizes this principle. Crucially, our formal analysis only establishes that this sign condition needs to hold within a specific range of errors around zero, rather than for arbitrarily large positional and gain errors. This follows from the local nature of our stability analysis, which investigates convergence within a neighborhood of zero error. However, if the sign condition in Eq. (7) never holds for any range of errors, then  $k_0$  simply cannot converge to  $k^*$ . On the other hand, as long as it holds within some range, recalibration is guaranteed—at least under the assumption of constant velocity. Later, we will numerically demonstrate that this constant-velocity assumption is likely not required, though a formal proof relaxing this assumption remains as future work.

Our analysis so far provided insights into complete recalibration of the PI gain. However, the data from<sup>33</sup> showed that, on average, the recalibration was only partial (75%). In such a case, the average PI gain  $k_0$  may converge to a value  $k_0^\infty$ , which is biased towards, but not necessarily equal to, the visual gain  $k^*$ . In turn, if  $k_0^\infty \neq k^*$ , the system may operate under some persistent, residual positional error  $\bar{\theta} = \bar{\theta}^\infty$  that is not equal to zero. The question is whether the conditions for complete recalibration also apply to partial recalibration. Assuming that the landmark-correction  $\beta$  does not depend on the PI-gain, we found that the same necessary and sufficient condition (Eq. (7)) must still be satisfied, but now with respect to the residual positional error at steady-state  $\bar{\theta} = \bar{\theta}^\infty$  rather than with respect to the zero error as was the case of complete recalibration. See Supplementary Note 4.3 for details.

Below, we simulate Eqs. (5) and (6) along with two example PI-gain update rules  $(g_0)$  to numerically illustrate our analytical findings, especially how specific functional forms of  $g_0$  determine the recalibration outcome. Additionally, these simulations offer intuition and insights that inform the design of ring attractor networks capable of PI-gain recalibration, as instantiated in Section "Implementing PI-gain recalibration in a ring attractor".

**Example 1.** The simplest PI-gain update rule satisfying the sign condition (Eq. (7)) is

$$\frac{dk_0}{dt} = g_0(\tilde{\theta}, v) = \mu \,\tilde{\theta} \, v,\tag{8}$$

where  $\mu$  denotes a positive learning rate. Because adjustment of the PI gain ceases at zero positional error  $\tilde{\theta}$  under this rule, the system achieves complete PI-gain recalibration by reaching  $k_0^\infty = k^*$  (top row,

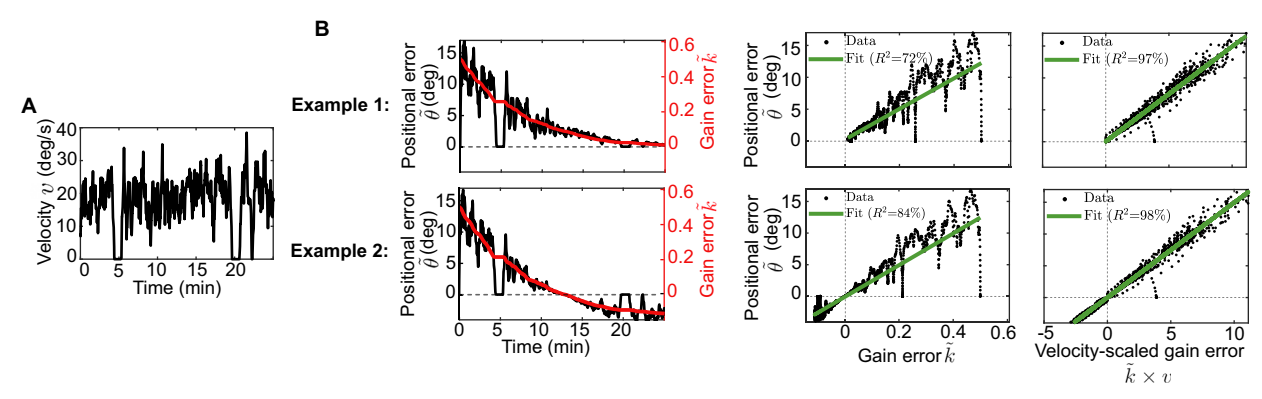


**Fig. 4** | **Numerical simulations of Eqs. (5) and (6) under two representative Plgain update rules given in Eqs. (8) and (9).** For both simulations, we set the initial condition  $k_0(0) = 1$ , the landmark stabilization function  $\beta(\bar{\theta}, k_0) = 0.66 \times \sin(\bar{\theta})$ , the visual gain  $k^* = 1.5$ , and the learning rate  $\mu = 0.02$ . The gain choices imply that the initial value of gain error is  $\bar{k}(0) = 0.5$ . Additionally, we chose the constant  $\eta = 0.12$  for the second example. **A** A smoothed velocity profile of an animal from an experiment in ref. 33. **B** It shows trajectories of the network's positional and gain errors (left column), their interrelationship (middle column), and how the animal's velocity influences this relationship (last column), all obtained from the simulation under the example Pl-gain update rules: Eq. (8) (Example 1, top row) and Eq. (9) (Example 2, bottom row). When the animal begins moving at t = 0, the positional error  $\bar{\theta}$  (black line, left *y*-axis) quickly increases because of the nonzero gain error  $\bar{k}$  (red line, right *y*-axis). As the Pl gain is modified, the gain error  $(\bar{k})$  and, consequently, the positional error diminishes gradually, eventually converging to steady

state. Their steady-state values are zero for Example 1 (complete gain recalibration) while being nonzero for Example 2 (partial recalibration). The middle column shows that although positional error strongly depends on gain error, it is also influenced by other factors. This additional influence can also be observed in the positional error progression in the left column. Although there is a general gradual, convergent trend of the gain and positional errors, the positional error goes through many fast, transitory changes around this trend. Close inspection reveals that these fast changes are influenced by changes in the animal's velocity. For example, as animal slows down  $(v\downarrow)$  around minute 5, the positional error decreases  $(\tilde{\theta}\downarrow)$ , eventually becoming zero  $(\tilde{\theta}=0)$  with the animal coming to a stop (v=0). This behavior of the positional error is best explained by the multiplication of the gain error with the animal's velocity. The right column verifies this analytical expectation using simulation results.

Fig. 4B). This numerical example demonstrates that the sign condition (Eq. (7)) is sufficient for PI-gain recalibration even when the animal's velocity is not constant.

**Example 2**. Consider now a slightly more complex PI-gain update rule

$$\frac{dk_0}{dt} = g_0(k_0, \tilde{\theta}, v) = \mu \tilde{\theta} v + \mu \eta k_0 v^2, \tag{9}$$

where  $\mu$  denotes a positive learning rate as before, and  $\eta$  denotes a constant that controls the magnitude of the additional velocity-dependent term  $\eta k_0 v^2$ . This term practically acts as a positive bias on top of the simplest Pl-gain update rule (Eq. (8)) that satisfies the sign condition. As we will see in Section "Implementing Pl-gain recalibration in a ring attractor", when we introduce a modified ring attractor model, this update rule provides a more biologically plausible representation of Pl-gain recalibration in a ring attractor network than the simplest update rule in the previous example.

Note that with the modified update rule in Eq. (9), the sign condition in Eq. (7) remains satisfied—but now relative to a steady-state positional error that may be nonzero depending on the velocity-dependent bias term  $\eta k_0 v^2$ . The degree of recalibration also depends on the magnitude of this term. If  $\eta=0$ , for example, the bias is zero, and the update rule reduces to the rule in Example 1, resulting in complete recalibration (i.e.,  $k_0^\infty=k^*$ ). Otherwise, recalibration is only partial (bottom row Fig. 4B) with a steady-state gain error that is proportional to both  $\eta$  and the animal's velocity v (see Eq. (132) and the analysis afterward in Supplementary Note 7.2 for a derivation).

The need for an explicit error code to meet the algorithmic conditions for PI-gain recalibration. How can a ring attractor network mechanistically implement Eq. (7), the algorithmic sign condition for PIgain recalibration? To address this question, we investigate an analytical expression of the spatial average of the ring attractor network's PI gain,  $k_0$ , which can be simply obtained by averaging the PI gain  $k(\theta)$  in Eq. (4) over  $\theta$ . The resulting expression identifies a number of terms as possible neural loci for updating  $k_0$ : (i) the synaptic time constant  $\tau_c$ , (ii) the offset b in the central-to-rotation ring connections, (iii) the synaptic weight functions  $W_{v-cw}$ ,  $W_{v-ccw}$  of the velocity-to-rotation ring connections, (iv) the synaptic weight functions  $W_{cw-c}$ ,  $W_{ccw-c}$  of the rotation-to-central ring connections, (v) the slope parameters  $\alpha_{cw}$ ,  $\alpha_{ccw}$ quantifying the absolute value of the tuning slopes of velocity neurons, (vi) the function  $\hat{r}_c$  describing the central ring's persistent activity bump, and (vii) the functions  $\hat{r}_{cw}$ ,  $\hat{r}_{ccw}$  describing solutions to the rotation ring's persistent activity bump. Out of the seven terms, we consider the last five (iii-vii) as candidates driving the PI-gain recalibration within the ring attractor model via temporal changes, implicitly assuming that the first two terms, the synaptic time constant  $\tau_c$ and the offset b are "hardwired" (i.e., time-invariant).

The rationale behind excluding the first two terms arises, in part, from the limitations of our modeling approach. First, the rate-based model of the ring attractor network does not include any cellular and receptor details to capture possible temporal changes in the synaptic time constant  $\tau_c$ . Instead, our model includes  $\tau_c$  as a "lumped parameter" reduction of complex phenomena that govern the changes in membrane potential with ion flux through receptors; future work could use biophysical modeling (e.g., ion channel kinetics) to investigate how changes in  $\tau_c$  could contribute to PI-gain recalibration, but that is beyond the scope of the present study. Second, our model employs a simplified one-to-one connectivity between rotation and central rings, where each neuron in a rotation ring connects to only one neuron in the central ring with a fixed offset b. This contrasts with a one-to-all connectivity, which would be necessary to capture plasticity in b through gradual modulation of weights along the neural space.

We then analyzed the relationship between the temporal change in each of the remaining five candidate terms and the resulting temporal change in the PI gain  $k_0$ . Regardless of which term drives the changes in the PI gain, we find that rate-based encoding of the positional error  $\hat{\theta}$  is critical for the ring attractor network to implement the sign condition (Eq. (7)), which is both necessary and sufficient for PIgain recalibration. However, the specific nature of the error code depends on the driver term. As we shall show, if the PI-gain recalibration is implemented by plastic changes in the velocity pathway of the circuit (iii-iv), then the error signal must take the form of a rate code for the *instantaneous difference* between  $\theta^*$  and  $\theta$ . In contrast, if the recalibration is implemented elsewhere in the circuit (v-vii), then the error signal must take the form of a rate code for the time integral of the error between  $\theta^*$  and  $\theta$ . Finally, it should be noted that these findings are derived using our previous analytical results (Eqs. (4-7)) and are therefore subject to the same assumptions.

Recalibration via plasticity in the velocity pathway is supported by a rate code of the instantaneous positional error. As previously implied in Section "The need for an explicit error code to meet the algorithmic conditions for PI-gain recalibration", the PI gain can be altered by modifying the strength of the velocity-dependent synaptic inputs onto the central ring. To this end, we first consider a mechanism that adjusts the ring attractor's PI gain through Hebbian plasticity in the pathway from velocity neurons to the central ring. This pathway includes the synaptic weight pair  $W_{v-cw}$ ,  $W_{v-ccw}$ , describing the strength of velocity-to-rotation ring connections (4 in Fig. 2A), and the pair  $W_{\text{cw-c}}$ ,  $W_{\text{ccw-c}}$ , describing the strength of rotation-to-central ring connections (3 in Fig. 2A). According to Eq. (4), the CW and CCW components of these weight pairs influence the PI gain in an additive manner. Because of the aforementioned CW-CCW symmetry requirement in Section "The need for an explicit error code to meet the algorithmic conditions for PI-gain recalibration" (i.e., the inputs to the central ring must be balanced for stability of PI during immobility periods), however, we assume that the CW and CCW components undergo the same temporal changes, ensuring that their individual contribution to PI remains symmetric. This symmetry assumption implies that if the value of  $k_0$  changes as per the algorithmic sign condition in Eq. (7), then the individual contribution of CW and CCW components must be in the direction of the product of the animal's velocity v and the positional error  $\tilde{\theta}$ . To identify the mechanistic underpinnings of such symmetric recalibration of the PI gain's spatial average  $k_0$ , we revisit Eq. (4). By differentiating this equation with respect to time and considering Hebbian plasticity in the velocity pathway, we find that the algorithmic condition translates into a mechanistic constraint as follows:

Hebbian plasticity of the velocity-to-rotation ring connections  $(W_{v-cw}, W_{v-ccw})$ : Controlling the strength of velocity inputs onto the ring attractor, these weights directly affect the movement speed of the activity bump for a given movement speed of the animal. This effect is locally instantiated as the weights are spatially distributed across the ring. Thus, when Hebbian plasticity modifies the weights  $W_{v-cw}$ ,  $W_{v-ccw}$  in a spatially inhomogeneous manner—due to unequal activation of neurons across the bump—movement speed of the bump begins to exhibit local variations depending on its location along the ring. As a result, the PI gain is updated non-uniformly. Despite these local variations, however, the *spatial averages* of the weights  $W_{v-cw}$ ,  $W_{v-ccw}$  always remain positively correlated with the *spatial average*  $k_0$  of the PI gain.

The fact that  $k_0$  is proportional to average strengths of these synapses constrains the mechanisms by which their Hebbian plasticity can achieve recalibration. Specifically, satisfying Eq. (7)—a necessary and sufficient condition for PI-gain recalibration—requires that the rate of change of the average strengths of these synapses must be in the same direction as the product of the animal's velocity (v) and the

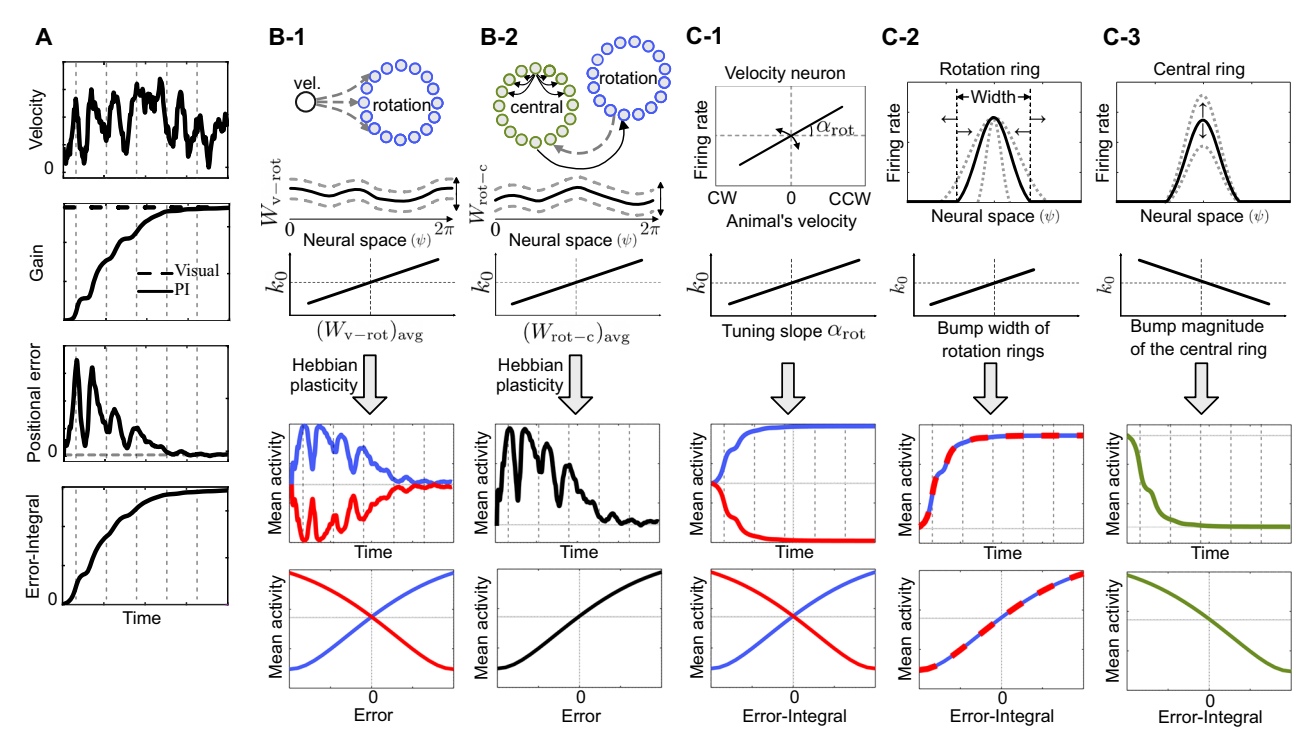


**Fig. 5** | **Neural mechanisms of Pl-gain recalibration based on a numerical simulation of Eqs. (5) and (8). A** Temporal progression of the animal's velocity v (from an experiment<sup>33</sup>) and other variables: gain  $(k_0)$ , positional error  $(\bar{\theta},$  and the time-integral of the error. Model parameters and initial conditions are the same as Example 1 in Fig. 4B. Similar to that example, the positional error reduces, as the system recalibrates its Pl gain. **B** Mechanistic constraints for recalibration through plasticity in the velocity pathway. (B-1) and (B-2) correspond to plasticity in the velocity-to-rotation ring and in the rotation-to-central ring connections, respectively (for simplicity, only one rotation ring is shown.). The weight profiles of these connections— $W_{v-rot}$  and  $W_{rot-c}$  (solid lines)—may be modified through Hebbian plasticity (dashed lines). The average Pl gain  $k_0$  remains positively correlated with their average strengths. B-1: If Hebbian plasticity modifies  $W_{v-rot}$  to drive  $k_0$  toward the visual gain  $k^*$ , then the mean firing rates of CCW (blue) and CW (red) rotation rings must vary over time, inversely with one another, to encode the instantaneous

positional error (bottom row of B-1). B-2: Alternatively,  $W_{\rm rotc}$  is modified, the mean firing rates of either the rotation or the central rings must vary to encode the same positional error (bottom row of B-2). Unlike B-1, our analysis does not determine the direction of this error-dependent variation in B2, so the direction of the depicted tuning curve is arbitrary. **C** Mechanistic constraints for recalibration via other mechanisms; each row follows a similar schema as the mechanisms in B: (C-1) Velocity neurons' slopes as the locus of plasticity. (C-2) Rotation rings' widths as the locus of plasticity. (C-3) The central ring's bump magnitude as the locus of plasticity. If the average PI gain  $k_0$  converges to  $k^*$  through changes in any of these neural loci, then the time-integral of the error must be encoded in the mean firing rates of a ring population. In the case of C-1 and C-2, CCW (blue) and CW (red) rotation rings are the sources of this integral-of-error rate code. In the case of C-3, the central ring (green) is the source. Note that the directions of these error codes (i.e., the tuning-curve slope) flip if the animal moves in the the opposite direction than panel **A**.

network's positional error  $(\hat{\theta})$ , namely:

$$\operatorname{sign}\left[\frac{d}{dt}(W_{v-cw})_{avg}\right] = \operatorname{sign}\left[\frac{d}{dt}(W_{v-ccw})_{avg}\right] = \operatorname{sign}[\tilde{\theta}v]. \tag{10}$$

Because the pre-synaptic side of these synapses consists of velocity neurons whose firing rates vary monotonically with the animal's velocity v, Hebbian plasticity can satisfy the above equality only if the firing rates of the post-synaptic neurons, namely, the rotation rings, similarly *exhibit a monotonic relationship with the instantaneous positional error*,  $\tilde{\theta}$  (Fig. 5B-1). This required error tuning within the CW and CCW rotation rings must also reflect the differential sign of velocity tuning within the CW and CCW velocity neurons (previously shown in Fig. 2D) to ensure that both CW and CCW pathways satisfy Eq. (10).

Intuitively, this error-rate code within the rotation rings enables the network to detect whether it is lagging behind or advancing ahead of reality, which in turn recruits Hebbian plasticity to adjust the strength of the synapses controlling the movement speed of the bump, effectively "speeding it up" or "slowing it down" as needed. Over time, this adaptive adjustment will result in recalibration of the PI gain. See Supplementary Note 5.1 for mathematical details.

Hebbian plasticity of the rotation-to-central ring connections  $(W_{\text{CW-c}}, W_{\text{CCW-c}})$ : Just as the velocity-to-rotation ring synapses can

recalibrate the PI gain through locally occurring Hebbian plasticity, the rotation-to-central ring connections ( $W_{\text{cw-c}}$ ,  $W_{\text{ccw-c}}$ ) can also contribute to its recalibration. In both cases, plasticity occurs in a spatially inhomogeneous manner due to the non-uniform activation of neurons across the bump. Fortunately, just as we saw for the velocity-to-rotation ring connections, the average strength of the rotation-to-central ring synapses remains positively correlated with the spatial average  $k_0$  of the PI gain.

Therefore, as in the previous case, if the network satisfies Eq. (7)—a necessary and sufficient condition for recalibration—via Hebbian plasticity of rotation-to-central ring synaptic weights  $W_{\text{cw-c}}$ ,  $W_{\text{ccw-c}}$ , then it must modify their average strengths in the same direction as the product of the network's positional error and the animal's velocity. In the case of velocity-to-rotation ring synapses, meeting this requirement necessitated a rate code for error on the postsynaptic side, since the pre-synaptic neurons were assumed to encode only velocity. Here, however, neither side of the rotation-tocentral ring connections is inherently constrained in this way, meaning that the positional error could, in principle, be encoded on either the pre- or post-synaptic side, provided that the velocity is also encoded. This encoding can occur in two ways: either the firing rate of a single ring (rotation or central) varies monotonically with both negative and positive instantaneous errors (Fig. 5B-2), or each ring exhibits monotonic tuning for only one direction of error, such that together they cover the full range. Mathematical details are provided in Supplementary Note 5.2.

As we prove in the relevant Supplementary Notes (referenced above). Hebbian plasticity in a component of the velocity pathway cannot modify the PI gain  $k_0$  as required by the algorithmic sign condition in Eq. (7), unless the firing rates of either the rotation rings or the central ring encode the instantaneous positional error via monotonic changes. Since this sign condition was previously identified as both necessary and sufficient for PI gain-recalibration in a ring attractor network (Section "Control theory reveals algorithmic conditions for PIgain recalibration"), it follows that a rate-coded representation of the network's instantaneous error is equally essential for PI-gain recalibration through Hebbian plasticity in the velocity pathway. Once the network includes both a rate code of the instantaneous positional error and Hebbian plasticity in the velocity pathway, synaptic weights undergo activity-dependent modifications that integrate this error signal over time. Consequently, the weights gradually track the time integral of the positional error, which serves as a proxy for the PI gain (Fig. 5A), ultimately recalibrating the PI gain. Put differently, the synaptic weights continuously accumulate past discrepancies, enabling the ring attractor network to fine-tune its PI gain dynamically.

Plasticity elsewhere is supported by a rate code of the time-integral of the error. We next consider the scenario where the synaptic weights along the velocity pathway are hardwired (i.e., constant). Instead, PIgain recalibration is driven by temporal changes in one of the three *firing-rate* related terms. These terms include the parameters  $\alpha_{cw}$ ,  $\alpha_{ccw}$ describing the absolute value of the velocity neurons' tuning slope, the ansatz functions  $\hat{r}_{\rm cw}$ ,  $\hat{r}_{\rm ccw}$  describing the rotation rings' activity bumps, or the ansatz  $\hat{r}_c$  describing the central ring's activity bump. In the previous case, where plasticity occurred in the velocity pathway, synaptic weights tracked the time-integral of the positional error through Hebbian modifications, ultimately recalibrating the ring attractor's PI gain. But how can the ring attractor achieve the same outcome in the absence of synaptic plasticity? As we show below, firing rates themselves varying according to the time-integral of the positional error is equally effective for PI-gain recalibration. Unlike synaptic plasticity in the velocity pathway, which recalibrates the PI gain through locally accumulating modifications, temporal changes in the firing-rate-related terms act globally across the neural space, ensuring that recalibration occurs uniformly, without introducing any spatial inhomogeneities into the PI gain.

Changes in the slopes of velocity neurons' tuning curves ( $\alpha_{cw}$ ,  $\alpha_{ccw}$ ): The slopes of velocity neurons' tuning curves determine how strongly they respond to movement. If the network detects that its position estimate is consistently off, adjusting these slopes would allow it to scale its velocity signals accordingly, effectively "speeding up" or "slowing down" to better align with reality. This indicates a direct relationship between the PI gain and the slopes of velocity neurons. Indeed, such a relationship can be seen in Eq. (4) where the velocity neurons' absolute slope parameters  $\alpha_{\rm cw}$ ,  $\alpha_{\rm ccw}$  act as a positive multiplicative factor on the value of the PI gain. Therefore, a change in these slope parameters leads to a commensurate change in the entire profile of the PI gain, thereby its spatial average  $k_0$  without introducing any inhomogeneities. Because this one-to-one positive relationship is similar to the ones studied in the previous section (despite the difference in inhomogeneities), we can again infer that satisfying the algorithmic sign condition (Eq. (7)) for the PI-gain recalibration is subject to the slope parameters  $\alpha_{cw}$ ,  $\alpha_{ccw}$  varying in the direction of the product of the animal's velocity (v) and the network's positional error  $(\theta)$ , namely,

$$\operatorname{sign}\left[\frac{d}{dt}\alpha_{\mathrm{cw}}\right] = \operatorname{sign}\left[\frac{d}{dt}\alpha_{\mathrm{ccw}}\right] = \operatorname{sign}[\tilde{\theta}\,\nu]. \tag{11}$$

This requirement implies that, when the animal is moving in one direction (as was the case in the recalibration experiments<sup>33</sup>), the *change in the slope parameters* is monotonically related to the positional error, reflecting its value on a moment-to-moment basis with a sign additionally depending on the sign of the velocity. As the velocity signals are transmitted to the rotation rings via synaptic connections, gradual changes in their tuning slopes—driven by instantaneous positional error—accumulate over time, leading to cumulative adjustments in the firing activity of the rotation rings. Consequently, the mean firing rate of the rotation rings reflects the accumulated positional error over time, *varying monotonically with the time-integral of the error* (Fig. 5C-1). Mathematical details are provided in Supplementary Note 5.3.

Changes in the persistent activity bump of the rotation rings  $(\hat{r}_{\text{cw}},\hat{r}_{\text{ccw}})$ : The rotation rings are responsible for providing the central ring with the movement signals from the velocity neurons, which in turn shifts the activity bump in tandem with the animal's movement. Intuitively, each rotation ring neuron acts like a pulley, transmitting the 'force' from a velocity neuron to its counterpart in the central ring, which eventually moves the activity bump. Hence, as more rotation ring neurons become active (i.e., wider rotation-ring bump  $\hat{r}_{cw}$ ,  $\hat{r}_{ccw}$ ), they provide broader synaptic input to the central ring, effectively amplifying the 'pulling force' on the activity bump. This results in a greater movement speed of the bump overall, leading to a commensurate increase in the PI gain globally without introducing any spatial inhomogeneities. By analyzing Eq. (4) in Supplementary Note 5.4, we indeed find a positive relationship between the widths of the rotation rings' activity bumps and the average PI gain  $k_0$ . This positive relationship is similar to the previous case regarding the slope parameters  $\alpha_{\rm cw}$ ,  $\alpha_{\rm ccw}$ . Thus, like in the previous case, satisfying Eq. (7) requires the rotation rings' activity widths to vary monotonically with the product of the animal's velocity and the positional error. Consequently, when the animal is traveling in one direction (say forward), the widths of the rotation rings' activity bumps must increase monotonically with the time-integral of the error (Fig. 5C-2). All else being equal, this implies a similar monotonic increase in the average firing rate of rotation rings with the time-integral of the error. The direction of this monotonic relationship is reversed if the animal moves in the other direction. See Supplementary 5.4 for mathematical details. Despite its similarity to the previous mechanisms in requiring a rate code of error, the present mechanism slightly differs in its capacity to recalibrate the PI gain. Unlike previous mechanisms, which in principle has no obvious limits on the range of values PI gain can be recalibrated to, the present mechanism, which involves changes to the rotation rings' bump widths, is inherently constrained. The maximum bump width is limited by the circular topology and its assumed relation with the central ring's bump width (Assumption 2 in SI).

Changes in the persistent activity bump of the central ring  $(\hat{r}_c)$ : Consider as an example that there are two networks with the same Gaussian bump profile but one has a higher peak firing rate. In this case, if all else is equal, the network with the higher firing requires higher velocity inputs to shift its activity bump from point A to point B at the same time as the other network (analogous to the greater force required to move a more massive object). This need for higher velocity inputs independent of the bump location indicates an inversely correlated relationship between the central ring's bump magnitude and the PI gain's value at all locations, thus its average  $k_0$ . This relationship can also be verified from Eq. (4) wherein the denominator includes a term proportional to the bump magnitude, which itself is positively correlated with the central ring's mean firing rate. Thus, satisfying the algorithmic condition for PI-gain recalibration is subject to a mechanistic constraint that is similar to the previous case in spirit but slightly different due to the inverse effect: When the animal is traveling in the positive direction, the central ring's average firing rate must decrease monotonically with the time-integral of the error (Fig. 5C-3).

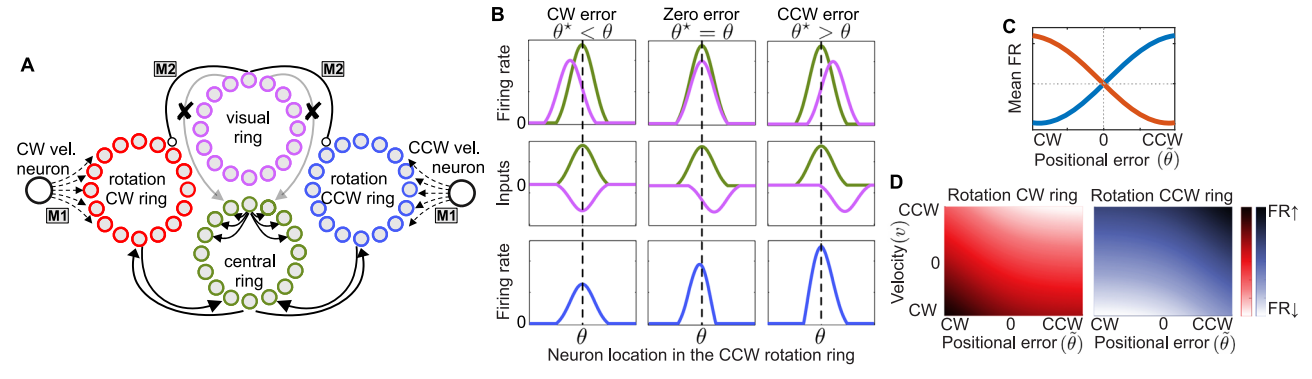


**Fig. 6** | **A modified ring attractor network model. A** Schematic representation of the model. Solid and dashed lines denote hardwired and plastic connections, respectively. Arrow and circle terminals denote excitatory and inhibitory connections, respectively. The labels M1 and M2 correspond to the two modifications made to the classical model. **B** Illustration of how CCW rotation ring's firing rate (blue) varies monotonically with the positional error ( $\theta^* - \theta$ ). Middle column: Zero error ( $\theta^* = \theta$ ). Although the visual ring's activity bump is aligned with that of the central ring (top row) in this error-free state, the CCW offset in the visual-to-CCW rotation ring connections introduces some misalignment between the inputs to the CCW rotation ring (middle row), resulting in moderate activity levels (bottom row). Left column: CW error ( $\theta^* - \theta < 0$ ). In this case, the visual-ring bump associated with  $\theta^*$  is shifted CW relative to the central-ring bump associated with  $\theta$  (top

row). Because of the CCW offset in the visual-to-CCW rotation ring connections, the inhibition from the visual ring becomes more aligned with the excitation from the central ring at the level of synaptic inputs (middle row), thereby reducing the firing rate of the CCW rotation-ring bump (bottom row). Right column: CCW error  $(\theta^* - \theta > 0)$ . Here, the visual-ring bump associated with  $\theta^*$  is shifted CCW relative to  $\theta$  (top row), and the CCW offset in the visual-to-CCW rotation ring connections places inhibition further away from the CCW rotation ring's active neurons (middle row), thereby increasing the firing rate of the rotation-ring bump (bottom row). C Tuning curve depicting the relationship between the rotation rings' mean firing rate and the positional error for a given velocity. The color coding is the same as in panel **A. D** Illustration of how CW (left) and CCW (right) rotation rings' firing rates depend conjunctively on the animal's velocity and the positional error.

Change in the movement direction reverses the direction of this relation. See Supplementary Note 5.5 for details.

As proved in the relevant Supplementary Notes (referenced above), a ring attractor network with a hardwired velocity pathway and a fixed synaptic time constant  $\tau_c$  and connection offset b cannot modify its PI gain  $k_0$  as required by the algorithmic sign condition in Eq. (7), if none of its rings encode the time-integral of the error as described above (i.e., if they all remain invariant relative to the timeintegral of error). Given that the sign condition is necessary for PI-gain recalibration, this finding indicates that a rate code of the time-integral of the positional error is equally essential for PI-gain recalibration in a ring attractor network lacking plasticity in its velocity pathway, synaptic time constant, and connection offset. While our analysis does not determine the precise mechanisms for generating such a rate code or the specific temporal variations in related terms (e.g., the slopes of velocity neurons), our findings do not rule out the possibility that some form of plasticity elsewhere in the network may be necessary to achieve them. Regardless of the underlying mechanism, however, the PI gain is no longer encoded in the synaptic weights: instead, it is encoded within the firing rates that track the time-integral of the error, a proxy of the PI gain (Fig. 5A). Taken together with our previous findings, we conclude that a rate code of the instantaneous positional error or its time integral is crucial to recalibrate the PI gain of a ring attractor network with a fixed synaptic time constant  $\tau_c$  and connection offset b.

#### Implementing PI-gain recalibration in a ring attractor

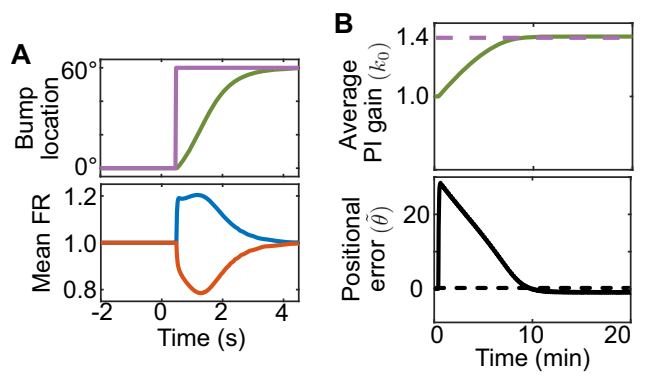
In this section, we propose a ring attractor network model to achieve Pl-gain recalibration through a mechanism developed from our theoretical findings. Briefly, the model utilizes plasticity in the velocity pathway and its mechanistic prerequisite: a rate code for the instantaneous positional error. Like classical models, the proposed model also corrects accumulated Pl errors based on feedback from landmarks. As described in the following subsections, we develop this model from the classical ring attractor network by introducing two specific modifications to its extrinsic connectivity. These modifications enable gain recalibration by inducing inhomogeneous synaptic weight changes that gradually fade as the Pl gain approaches its target value. Additionally, we present a conceptual model in Supplementary

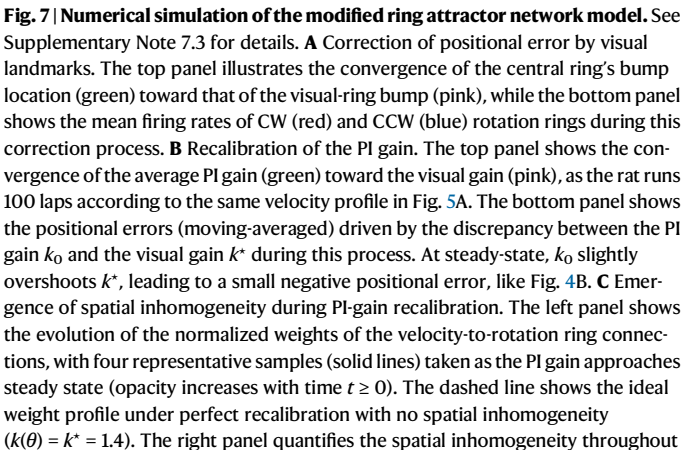
Note 6 that recalibrates its PI gain without relying on any synaptic plasticity. Instead, it adjusts the activity bump's magnitude based on the time-integral of the error, as illustrated in Fig. 5C-3, that is encoded by a line attractor<sup>53-55</sup>. Unlike the detailed model described in the rest of the present section, this conceptual model applies gain adjustments globally, ensuring that the PI gain remains spatially homogeneous at all times. Together, these models demonstrate how explicit error coding at the level of individual neurons can support PI-gain recalibration and highlight the robustness of our theoretical results across different implementation approaches.

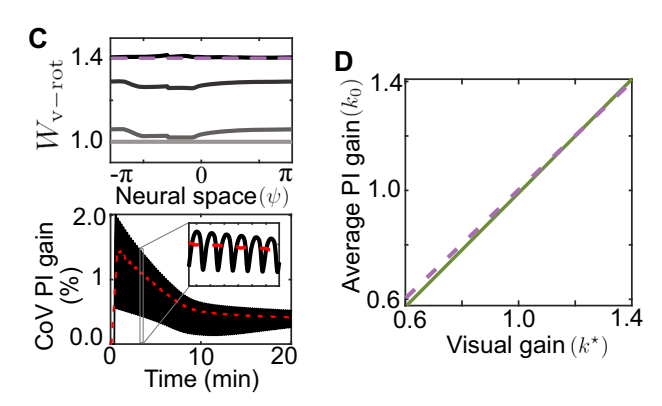
**Connectivity modifications.** We begin by adding Hebbian plasticity into the velocity-to-rotation ring connections of the classical ring attractor network (MI in Fig. 6A). Based on our theoretical results, specifically Fig. 5B-1, we know that recalibrating PI gain through this plasticity requires CCW and CW rotation rings to respectively increase and decrease their firing rates monotonically with the instantaneous positional error in the network's representation.

In the classical ring attractor, the visual drive—a necessary component for computing these error codes—is provided to the central ring via topographic excitatory connections. However, this setup is incompatible with the required properties of the error codes in two aspects: First, because the CCW and CW rotation rings derive their activity bump from the central ring via symmetric connections, the classical model's visual drive cannot change them in distinct directions (e.g., an increase in CCW accompanied by a decrease in CW with error), as required by the aforementioned error code. Second, because topographic connections within the classical model align the visual drive symmetrically with the attractor's activity bump in the absence of errors, positive and negative positional errors affect the attractor's average firing rate similarly (e.g., both error directions lead to an increase), failing to induce the required monotonic changes.

To overcome these limitations of the classical ring attractor, we remove the topographic connections between the visual and the central rings and introduce *offset* inhibitory connections from the visual ring onto the rotation rings (M2 in Fig. 6A). Specifically, we connect the visual ring to the CCW rotation ring with a *CCW offset* and to the CW rotation ring with a *CW offset*. Note that these offset connections are distinct from the existing offset connections







the recalibration process with the coefficient of variation (CoV) across the circular neural space (black line; with moving average in red). At the start of the simulation, weights near the bump's initial location are upregulated locally, increasing inhomogeneity. As the bump moves, synaptic changes propagate to other regions, gradually reducing inhomogeneity. However, because the bump cycles through the neural space, this process repeats each lap, creating periodic fluctuations in spatial inhomogeneity (black line) at the same frequency as the bump's traversal. As recalibration progresses and the PI gain nears its target, the magnitude of these synaptic adjustments diminishes, leading to a gradual stabilization of inhomogeneity. D The relationship between the PI and visual gains (green line) in comparison to the perfect recalibration case (dashed pink line). Observe the subtle asymmetry in this simulated relationship. The simple algorithmic model previously simulated based on Eq. (9) as well as our analyses of the modified network model in Supplementary Note 7.2 and Supplementary Fig. 7 predict a similar asymmetry due to the asymmetric influence of the squared velocity term on the steady-state PI gain. Interestingly, similar asymmetries have been observed experimentally<sup>23,33,94</sup>.

between the rotation and central rings. Unlike the existing rotationto-central ring connections that implement PI, the newly added equal and opposite offset connections between the visual and rotation rings enable the CCW and CW rotation rings to increase and decrease their firing rates, respectively, as a monotonic function of the network's positional error (Fig. 6B, C). However, in networks with a narrow visual ring bump, this monotonic relationship is maintained only within a limited range of positional errors: once the positional error exceeds a certain threshold (which increases with the visual ring's bump width), the inhibitory visual inputs escape the excitatory input from the central ring's activity bump, rendering the rotation rings' firing rates insensitive to further errors (Supplementary Fig. 6A-B). Nevertheless, as we show next the system automatically corrects errors as they occur, preventing them from accumulating, thereby helping the rotation rings maintain their error code within the monotonic range.

Correction of errors by landmarks. A well-known feature of classical ring attractor networks is their ability to correct PI errors based on the excitatory visual drive onto the central ring as we model in Section "The visual ring provides gain-dependent positional feedback that corrects path integration" (remember the  $\beta$  function). With the inhibitory offset connections onto the rotation rings replacing the original excitatory ones onto the central ring, an important question is whether our model retains its landmark correction capability. As shown in Fig. 6C, this replacement results in differential modulation of the rotation rings' firing rates by the positional error. This modulation resembles how velocity neurons affect the rotation rings: when the animal moves, the firing rate of one rotation ring increases while the other decreases, thereby shifting the activity bump along the central ring.

Thus, by encoding the positional error in directionally distinct rate codes within the rotation rings, our model effectively converts positional error into a "virtual velocity signal" which in turn shifts the activity bump along the central ring in a manner that reduces this error. We confirm this error correction mechanism in a numerical simulation of our model. Following an abruptly introduced positional error between the activity bumps of the central and visual ring, the differential changes in the rotation rings' firing rates successfully realign the central ring's activity bump with that of the visual ring, analogous to a "visual fix" (Fig. 7A). By continuously providing such a 'fix', this mechanism helps ensure that the system operates not only within the dynamic range of its error-rate code but also with minimal representational error. However, there are certain cases where this error correction mechanism may fail. For instance, if the positional error suddenly becomes too largeexceeding the width of the visual-ring bump-firing rates of CW and CCW rotation become nearly equal. In this case, they fail to generate an appropriate virtual velocity signal for realignment (Supplementary Fig. 6C). Interestingly, this apparent limitation of our model resembles experimental data from the rodent head direction and place cell systems, where cue conflicts exceeding a threshold (typically reported to be 45°-90°) led to a failure in realignment of the activity bump<sup>27,56-58</sup>.

**Recalibration of PI gain by landmarks.** In addition to correcting positional errors via error-rate codes within the rotation rings, our model is also capable of recalibrating its PI gain when these error-rate codes are paired with Hebbian plasticity in the velocity-to-rotation ring connections. Hebbian plasticity adjusts the synaptic weights based on the correlated activity of pre- and post-synaptic neurons. In the velocity-to-rotation ring connections, this adjustment occurs positively with the product of the animal's velocity v (encoded by both preand post-synaptic neurons) and the positional error  $\tilde{\theta}$  (encoded only by post-synaptic neurons), ensuring that the PI gain's spatial average  $k_0$ , which depends linearly on these plastic weights, varies according to  $\tilde{\theta} \times v$  as required by Eq. (7), the algorithmic condition for its recalibration.

While this algorithmic condition establishes PI-gain recalibration, it is unclear whether the model can reach a complete recalibration. where the PI gain's spatial average  $k_0$  would converge exactly to the visual gain  $k^*$ , or a partial recalibration, where  $k_0$  would converge to a value only biased towards  $k^*$ . As illustrated by the algorithmic Examples 1 and 2 in Section "Control theory reveals algorithmic conditions for PI-gain recalibration", complete PI-gain recalibration is achieved if no additional variable other than the product of the animal's velocity vand the network's positional error  $\tilde{\theta}$  influences the temporal change in the average PI gain  $k_0$ . However, in our modified model, the presynaptic side of the velocity-to-rotation ring connections solely encodes the animal's velocity v, whereas the rotation rings on the postsynaptic side additively encode the positional error  $\theta$  along with v(Fig. 6D). As a result, Hebbian plasticity modifies the synaptic weights not only by the product  $\theta \times v$  but also by the squared velocity  $v^2$ . As previously shown in Example 2 in Section "Algorithmic and mechanistic requirements for PI-gain recalibration", this additional  $v^2$  term implies that our model achieves only partial recalibration.

How close  $k_0$  gets to the visual gain  $k^*$  at the end of this partial recalibration depends on the relative contributions of  $v^2$  and  $\tilde{\theta} \times v -$  trade-off between the influence of error and velocity on the firing rates of the rotation rings. Specifically, as the positional error modulation of rotation rings' firing rates becomes more dominant relative to their velocity modulation, the influence of the  $\tilde{\theta} \times v$  term increases relative to the  $v^2$  term, enhancing the extent of the recalibration. To achieve such dominance of the error modulation, we propose two minor refinements in Supplementary Note 7.2 to the design of our modified ring attractor, based on computational and theoretical analyses: (i) using a sharper activity bump for the visual ring and (ii) incorporating weak inhibitory connections from the visual ring to the central ring. These minor refinements enhance gain recalibration without compromising error correction or path integration and are therefore employed in our simulation studies.

In simulation, we test the performance of PI-gain recalibration within our modified ring attractor network model for a simulated rat running on a circular track while visual landmarks were moved as per the visual gain  $k^*$ . The simulation confirms our theoretical expectations, showing that the network's PI gain  $k_0$  partially recalibrates to the visual gain  $k^*$ . During this recalibration, the PI gain inevitably and quickly becomes spatially inhomogeneous because of non-uniform weight changes from Hebbian plasticity across the neural space. As the animal continues to move under spatially uniform visual feedback from landmarks, however, these inhomogeneities within the PI gain gradually reduce, eventually reaching a minimal level at which point the PI gain closely approximates, though does not exactly match, the visual gain  $k^*$  at all locations in the neural space (Fig. 7B, C). Therefore, our modified ring attractor is capable of learning and maintaining a reasonably well-tuned PI gain for a range of visual gains based on feedback from landmarks (Supplementary Fig. 6D), unlike the classical ring attractor, which lacks any such recalibration behavior. That said, the recalibration may fail in our model if the discrepancy between the PI gain  $k_0$  and the visual gain  $k^*$  suddenly becomes very large, leading to positional errors  $\tilde{\theta}$  (recall from Fig. 4B that positional error is correlated with the gain error) greater than the dynamic range of the errorencoding scheme within the rotation rings. In such cases, our model breaks free from landmark feedback, unable to recalibrate its PI gain (Supplementary Fig. 6D). This simulated behavior aligns closely with the response of CA1 place cells under large gain changes as reported in ref. 33.

# Discussion

Fine-tuning the gain factor of a neural integration computation is crucial to maintain accurate representations of continuous variables since the relationship between the sensing of the relative change in a continuous variable and its actual value can fluctuate on both developmental (e.g., changes in body size<sup>59</sup>) and behavioral (e.g., changes in locomotion effort due to a change in locomotion surface<sup>60,61</sup>) time scales and even due to dynamic biological processes, such as circadian rhythms, that can alter synaptic transmission and intrinsic electrical properties of neurons<sup>62,63</sup>. Building upon previous behavioral work on perceptual plasticity of human locomotion<sup>30,64</sup>, experiments showed that a persistent conflict between self-motion and external visual cues recalibrates the integrator gain of hippocampal place cells, demonstrating the first physiological evidence for such fine-tuning<sup>33</sup>.

In the present paper, we investigated the algorithmic and mechanistic requirements for gain recalibration in a ring attractor network with a three-ring structure, a prevailing CBAN-type model for encoding circular continuous variables. In CBAN models, when the integration gain is inaccurate, an internal representation of a continuous variable slightly drifts relative to its actual value, resulting in encoding errors. When absolute 'ground-truth' information (e.g., feedback from visual landmarks in the present study) is present, the representational errors are corrected automatically through the CBAN's internal dynamics, without any need for an explicit code of the error at the level of single neurons. In contrast to this automatic error correction, our findings, conceptually summarized in Fig. 8, provide strong theoretical evidence that fine-tuning the integration gain of a CBAN may critically depend on an explicit error signal encoded within the firing rates of individual neurons. Overall, our results suggest a new role for brain circuits hypothesized to form a CBAN and highlight a critical modification to prior CBAN models, which lack such an explicit error signal. Beyond gain recalibration, this type of explicit error signal could serve a more generalized function supporting novelty detection, assessing the reliability of absolute information from external cues, and building an internal sense of confidence in the accuracy of the encoded continuous variable-potentially informing planning and decision-making in complex behavioral tasks.

## Limitations

Although our findings have been obtained through a detailed analysis of a ring attractor, certain assumptions were made for mathematical tractability, introducing limitations to our study. First, we examined a ring attractor network with a three-ring topology<sup>8</sup>, a choice supported by strong experimental evidence<sup>18,19</sup> and its adoption as the classical model for spatial representations in 1D and 2D<sup>36,44</sup>. Although our findings can be readily generalized to CBANs with the same topology in higher dimensions, they may not extend as readily to CBANs with different topologies, such as double-ring attractors<sup>12</sup>. Second, we used a dimensionality reduction technique to derive a simplified model of the ring attractor, based on which we identified the algorithmic conditions for PI-gain recalibration. This reduction provides an accurate approximation when external inputs to the attractor are relatively weak compared to its internal dynamics and when the activity bump is symmetric and lives on a continuum. If these assumptions fail, the accuracy of the reduced model degrades, in which case our findings may become less relevant to the network's actual dynamics. For instance, smaller networks, such as the putative attractor of the fly head direction system, may violate some of these assumptions. Third, we carried out local stability analysis to derive the necessary conditions for PI-gain recalibration. Although our analysis established a rate code of the attractor's positional error as such a condition, it did not identify the dynamic range of this encoding scheme because of its local nature, except that the dynamic range must encompass zero error. Fourth, our search for the mechanistic requirements for PI-gain recalibration was based on an exhaustive analysis of the relationship between the model parameters of a ring attractor and the value of its PI gain. In doing so, however, we excluded two parameters, namely the synaptic time constant and the value of the offset in the central-to-rotation ring connections, because of our

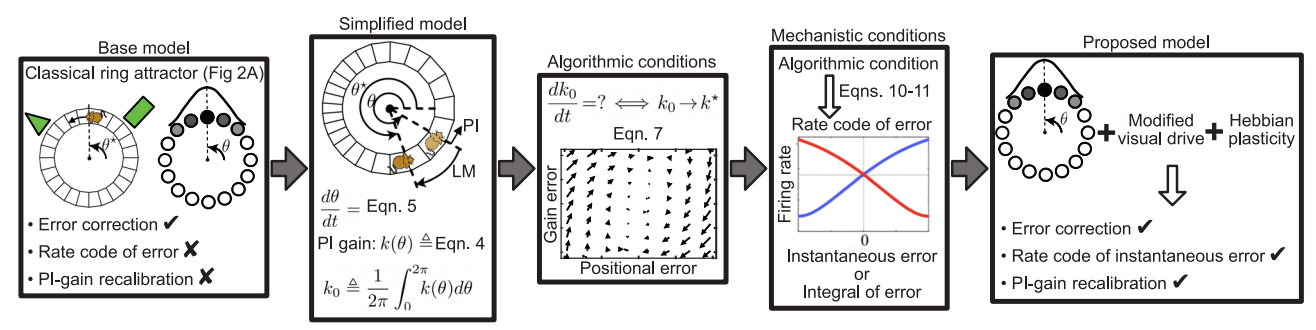


**Fig. 8** | **Snapshot of our key findings, approach, and paper organization.** We modeled the spatially tuned activity of hippocampal place cells on the circular track surrounded by landmarks (LM, green objects) as a classical ring attractor network. This classical model lacks an explicit error code and the ability to recalibrate its integration gain, referred to as path-integration (PI) gain in the context of spatial coding. To garner insight into the neural mechanisms that can achieve this recalibration, we first performed a dimensionality reduction in Section "Model setup: ring attractor network". This reduction led to an analytical expression of the PI gain k along with a simple dynamical model of how the location  $\theta$  of the network's activity bump is controlled by LM and PI. In contrast to previous work implicitly assuming that CBANs' integration gain is a global parameter, we found that a ring attractor network's integration gain is a spatially distributed parameter. Under certain conditions outlined in Section "The need for an explicit error code to meet the algorithmic conditions for PI-gain recalibration", this spatially distributed parameter can become inhomogeneous, varying as a function of the bump

location. We then employed control theory techniques in Section "Control theory reveals algorithmic conditions for Pl-gain recalibration" to dissect the algorithmic conditions for how the spatial average  $k_0$  of this distributed integration gain can be recalibrated to a target value  $k^*$  and how zero positional error can be achieved, together forming a 2D stable dynamical system as exemplified by the phase portrait. Mapping these conditions from the abstract, algorithmic level to the network level in Section "The need for an explicit error code to meet the algorithmic conditions for Pl-gain recalibration", we found strong theoretical evidence that, under many conditions, Pl-gain recalibration in a ring attractor network requires some neurons' firing rates to encode either the instantaneous positional error or its time integral. Finally, in Section "Implementing Pl-gain recalibration in a ring attractor", we propose a ring attractor network with modified extrinsic connectivity and Hebbian plasticity as an example CBAN model that can recalibrate its Pl gain based on such an explicit error code.

model's inability to include details about how they may change, as explained in Section "The need for an explicit error code to meet the algorithmic conditions for PI-gain recalibration". Thus, while it remains an open question, PI-gain recalibration may be influenced by the plasticity of the excluded parameters, in which case our findings may not be applicable. We leave the investigation of these limitations as future work.

# Continuous bump attractor network as an adaptive Kalman filter

To identify algorithmic requirements for recalibration of the integration gain, we simplified the dynamics of the ring attractor through a dimensionality reduction protocol described in<sup>39,45,46</sup>. Similar approaches have recently been applied to explore the evolution of high-dimensional neural data within low-dimensional structures<sup>6,15,65</sup>. In our case, the dimensionality reduction yielded a simplified 1D model of the ring attractor, capturing its response to both differential inputs (e.g., velocity) and absolute positional feedback from landmarks<sup>45,46,66</sup>.

Previous studies demonstrated that when multiple cues are presented as inputs, the ring attractor network can, under certain conditions and mechanisms, approximate Bayes-optimal cue fusion<sup>22,67-70</sup>. If one of the cues provides only differential information, such as an animal's velocity, the network recursively integrates and fuses the information, performing a Kalman-like filtering process at each integration step<sup>45</sup>. In standard Kalman filtering, such integration depends on a fixed internal model that assumes stable parameters (see ref. 67 for a neural implementation of the standard Kalman filter). In contrast, our analysis suggests that a ring attractor with PI-gain recalibration acts as an adaptive Kalman filter, continuously tuning its integration gain over time. To achieve this adaptive tuning, our model follows a specific algorithmic rule: the integration gain must change in the same direction as the product of the animal's velocity and the model's positional representation error relative to the external reference. This rule aligns closely with principles from adaptive control in engineered systems, where similar multiplicative mechanisms, like those in the MIT rule 1, guide parameter adaptation.

# The need for explicit error signals in the continuous bump attractor networks

Our theoretical analysis provided evidence that rate-based encoding of the instantaneous value or the time-integral of the representational error at the level of single neurons may play a critical role in the recalibration of the integration gain within CBAN models. Intuitively, without such explicit error-rate codes, the network does not have a teaching signal that can guide the tuning of its integration gain. This implies that, for CBAN models, learning the integration gain from errors can be a very different neural process than correcting the errors, which can occur automatically through network dynamics.

The hypothesized explicit error signal resembles reward and sensory prediction error signals within the mammalian brain. Midbrain dopamine neurons encode error in the internal predictions of reward via monotonic changes in their firing rates<sup>72,73</sup>; they elevate their activity with more reward than predicted, remain at baseline activity for fully predicted rewards, and exhibit depressed activity with less reward than predicted. Climbing fiber inputs to Purkinje cells of the cerebellum encode errors in the predicted sensory consequences of motor commands via changes in the rate and duration of complex spikes<sup>74,75</sup>. Both midbrain and cerebellar rate-based error codes are thought to act as teaching signals that recalibrate the internal models, just like how a rate-based error code can act as a teaching signal that recalibrates the integration gain of a CBAN.

To demonstrate the practical relevance of our theoretical findings, we implemented explicit error codes in two distinct ring attractor models. The first is a detailed model, for which we showed through systematic simulations that it can recalibrate its integration gain based on a rate code of the instantaneous error combined with Hebbian plasticity. The second is a conceptual model describing a potential recalibration mechanism based on the time-integral of error without any synaptic plasticity. These biologically plausible models, inspired by our theoretical findings, represent advances over prior work, where biologically implausible or unproven plasticity rules were used for gain recalibration<sup>37,38</sup>. Moreover, unlike the prior work, which offered limited mechanistic insights, our work makes a concrete experimental prediction: errors between representations in a CBAN and absolute teaching signals must be encoded by the firing rates of some neurons

in the circuit. Testing for the presence of such error signals in brain circuits that are thought to form a CBAN remains future work.

#### Implications of a distributed integration gain

Prior CBAN models implicitly assumed the integration gain to be a single, global parameter of the network, independent of the value of the encoded continuous variable<sup>11,36</sup>. Although the idea of different, hard-wired integration gains has previously been suggested in the context of location coding to explain the changes in the spatial scale of place coding along the dorsal-ventral axis of the hippocampus<sup>29</sup>, it has largely been assumed that the integration gains are constant at all locations within an environment (but see ref. 45). In contrast, our analysis of a CBAN network showed that the integration gain is a spatially distributed parameter instantiated in the network's array of synaptic weights. If plasticity occurs in the synapses between the differential (e.g., velocity) inputs and the attractor during recalibration, this distributed gain may temporarily become inhomogeneous, taking on different values across different locations in the neural space (corresponding to different values of the encoded continuous variable). This transient inhomogeneity, which is contingent upon local synaptic plasticity in the pathway between differential inputs and the attractor, is a strong experimental prediction of our study. Under this prediction, we expect some regions of the hippocampal map to compress while others stretching, subtly warping how distances are represented across the neural manifold throughout the recalibration process (similar distance warping in place cells can be caused by the presence of texture boundaries on the local surface<sup>76</sup>).

Theoretically, spatial inhomogeneity may be a stable state of the system if the teaching signal (e.g., feedback from absolute 'groundtruth' information sources) is available nonuniformly across the values of the continuous variable (unlike the case we studied in Fig. 7B, C). As a result, a CBAN becomes capable of adjusting its representation metric locally (as in Fig. 3B), which promises flexibility in representing different values of the continuous variable with uneven resolutions. depending on, for instance, their behavioral significance<sup>77</sup>. This representational flexibility, driven by the attainment of the inhomogeneous integration gain as a stable state, may offer a mechanistic explanation for some experimental findings from spatial navigation and decision-making literature. In the context of spatial navigation, a CBAN can employ inhomogeneous integration gains to "overrepresent" certain locations, for instance nearby rewards or boundaries, as is seen in recordings from hippocampus and entorhinal cortex<sup>78-87</sup>. In the context of decision-making, a CBAN with such inhomogeneities can accumulate early or late evidence unevenly, reproducing the so-called primacy and recency effects in the decisionmaking literature<sup>88-90</sup>. Complementing the mechanisms proposed in prior work<sup>4,45</sup>, our finding regarding the inhomogeneous integration gain of CBANs offers an alternative explanation to an array of seemingly complex responses in spatial navigation as well as other brain functions.

In this manuscript, we investigated whether a CBAN can automatically recalibrate its integration gain without relying on an explicit error code-just as it does for error correction (Fig. 1). Our findings provide strong theoretical evidence that, unlike error correction, which emerges spontaneously from network dynamics, recalibration likely requires an explicit rate code of error at the level of individual neurons. This distinction highlights a fundamental difference between these two processes—error correction vs. integration gain recalibration—and underscores the general importance of explicit error coding in adaptive neural computation.

#### Methods

Detailed derivations, proofs, and implementation details are provided in the Supplementary Information materials, summarized below.

#### Theoretical analyses

- Supplementary Notes 1 to 3 cover derivation of the reduced ringattractor models introduced in Section "Model setup: ring attractor network.
- Supplementary Note 4 derives the general PI-gain recalibration rule and proves the necessary and sufficient conditions for its stability (Section "Control theory reveals algorithmic conditions for PI-gain recalibration").
- Supplementary Note 5 proves the neural-mechanism requirements discussed in Section "The need for an explicit error code to meet the algorithmic conditions for Pl-gain recalibration".

#### **Computational analyses**

- Supplementary Note 6 introduces the conceptual ring-attractor model referred in Section "Implementing PI-gain recalibration in a ring attractor".
- Supplementary Note 7.2 details the design of the modified ringattractor model analyzed in Section "Implementing PI-gain recalibration in a ring attractor".
- Supplementary Note 7.3 describes the simulation procedures and parameter values.

#### **Reporting summary**

Further information on research design is available in the Nature Portfolio Reporting Summary linked to this article.

# **Data availability**

All data that support the findings of this study are publicly available at https://github.com/LIMBSlab/secer2025\_expliciterror.git. Source data are provided with this paper.

# **Code availability**

All code that support the findings of this study are publicly available at https://github.com/LIMBSlab/secer2025\_expliciterror.git.

#### References

- Ben-Yishai, R., Bar-Or, R. L. & Sompolinsky, H. Theory of orientation tuning in visual cortex. *Proc. Natl Acad. Sci.* 92, 3844–3848 (1995).
- Wimmer, K., Nykamp, D. Q., Constantinidis, C. & Compte, A. Bump attractor dynamics in prefrontal cortex explains behavioral precision in spatial working memory. *Nat. Neurosci.* 17, 431–439 (2014).
- Compte, A., Brunel, N., Goldman-Rakic, P. S. & Wang, X.-J. Synaptic mechanisms and network dynamics underlying spatial working memory in a cortical network model. *Cereb. Cortex* 10, 910–923 (2000).
- Esnaola-Acebes, J. M., Roxin, A. & Wimmer, K. Flexible integration of continuous sensory evidence in perceptual estimation tasks. *Proc. Natl Acad. Sci.* 119, e2214441119 (2022).
- Furman, M. & Wang, X.-J. Similarity effect and optimal control of multiple-choice decision making. *Neuron* 60, 1153–1168 (2008).
- 6. Nieh, E. H. et al. Geometry of abstract learned knowledge in the hippocampus. *Nature* **595**, 80–84 (2021).
- 7. Wojtak, W., Coombes, S., Avitabile, D., Bicho, E. & Erlhagen, W. A dynamic neural field model of continuous input integration. *Biol. Cybern.* **115**, 451–471 (2021).
- Skaggs, W., Knierim, J., Kudrimoti, H. & McNaughton, B. A model of the neural basis of the rat's sense of direction. *Adv. Neural Inf. Process. Syst.* 7, 173–180 (1994).
- Blair, H. Simulation of a thalamocortical circuit for computing directional heading in the rat. Adv. Neural Inf. Process. Syst. 8, 152–158 (1995).
- Redish, A. D., Elga, A. N. & Touretzky, D. S. A coupled attractor model of the rodent head direction system. *Netw. Comput. Neural* Syst. 7, 671–685 (1996).

- Zhang, K. Representation of spatial orientation by the intrinsic dynamics of the head-direction cell ensemble: a theory. *J. Neurosci.* 16. 2112–2126 (1996).
- Xie, X., Hahnloser, R. H. & Seung, H. S. Double-ring network model of the head-direction system. *Phys. Rev. E* 66, 041902 (2002).
- Knierim, J. J. & Zhang, K. Attractor dynamics of spatially correlated neural activity in the limbic system. *Annu. Rev. Neurosci.* 35, 267–285 (2012).
- Yoon, K. et al. Specific evidence of low-dimensional continuous attractor dynamics in grid cells. Nat. Neurosci. 16, 1077–1084 (2013).
- Gardner, R. J. et al. Toroidal topology of population activity in grid cells. Nature 602, 123–128 (2022).
- Ajabi, Z., Keinath, A. T., Wei, X.-X. & Brandon, M. P. Population dynamics of head-direction neurons during drift and reorientation. *Nature* 615, 892–899 (2023).
- Kim, S. S., Rouault, H., Druckmann, S. & Jayaraman, V. Ring attractor dynamics in the drosophila central brain. Science 356, 849–853 (2017).
- Green, J. et al. A neural circuit architecture for angular integration in drosophila. Nature 546, 101–106 (2017).
- Turner-Evans, D. et al. Angular velocity integration in a fly heading circuit. eLife 6, e23496 (2017).
- Turner-Evans, D. B. et al. The neuroanatomical ultrastructure and function of a biological ring attractor. Neuron 108, 145–163 (2020).
- Bicanski, A. & Burgess, N. Environmental anchoring of head direction in a computational model of retrosplenial cortex. *J. Neurosci.* 36, 11601–11618 (2016).
- 22. Jeffery, K. J., Page, H. J. & Stringer, S. M. Optimal cue combination and landmark-stability learning in the head direction system. *J. Physiol.* **594**, 6527–6534 (2016).
- Campbell, M. G. et al. Principles governing the integration of landmark and self-motion cues in entorhinal cortical codes for navigation. *Nat. Neurosci.* 21, 1096-1106 (2018).
- Muller, R. U. & Kubie, J. L. The effects of changes in the environment on the spatial firing of hippocampal complex-spike cells. J. Neurosci. 7, 1951–1968 (1987).
- Taube, J. S., Muller, R. U. & Ranck, J. B. Head-direction cells recorded from the postsubiculum in freely moving rats. ii. effects of environmental manipulations. J. Neurosci. 10, 436–447 (1990).
- 26. Goodridge, J. P., Dudchenko, P. A., Worboys, K. A., Golob, E. J. & Taube, J. S. Cue control and head direction cells. *Behav. Neurosci.* **112**, 749 (1998).
- Knierim, J. J., Kudrimoti, H. S. & McNaughton, B. L. Interactions between idiothetic cues and external landmarks in the control of place cells and head direction cells. *J. Neurophysiol.* 80, 425–446 (1998).
- Savelli, F., Luck, J. & Knierim, J. J. Framing of grid cells within and beyond navigation boundaries. eLife 6, e21354 (2017).
- Terrazas, A. et al. Self-motion and the hippocampal spatial metric. J. Neurosci. 25, 8085–8096 (2005).
- Tcheang, L., Bülthoff, H. H. & Burgess, N. Visual influence on path integration in darkness indicates a multimodal representation of large-scale space. *Proc. Natl Acad. Sci.* 108, 1152–1157 (2011).
- McNaughton, B. L., Battaglia, F. P., Jensen, O., Moser, E. I. & Moser, M.-B. Path integration and the neural basis of the cognitive map.'. Nat. Rev. Neurosci. 7, 663–678 (2006).
- 32. Shimbo, A., Izawa, E.-I. & Fujisawa, S. Scalable representation of time in the hippocampus. *Sci. Adv.* **7**, eabd7013 (2021).
- Jayakumar, R. P. et al. Recalibration of path integration in hippocampal place cells. *Nature* 566, 533-537 (2019).
- 34. Fuhs, M. C. & Touretzky, D. S. A spin glass model of path integration in rat medial entorhinal cortex. *J. Neurosci.* **26**, 4266–4276 (2006).
- Conklin, J. & Eliasmith, C. A controlled attractor network model of path integration in the rat. J. Comput. Neurosci. 18, 183–203 (2005).

- Burak, Y. & Fiete, I. R. Accurate path integration in continuous attractor network models of grid cells. PLoS Comput. Biol. 5, e1000291 (2009).
- 37. Hahnloser, R. Emergence of neural integration in the head-direction system by visual supervision. *Neuroscience* **120**, 877–891 (2003).
- 38. Vafidis, P., Owald, D., D'Albis, T. & Kempter, R. Learning accurate path integration in ring attractor models of the head direction system. *eLife* 11, e69841 (2022).
- 39. Amari, S.-i Dynamics of pattern formation in lateral-inhibition type neural fields. *Biol. Cybern.* **27**, 77–87 (1977).
- Noorman, M., Hulse, B. K., Jayaraman, V., Romani, S. & Hermundstad, A. M. Maintaining and updating accurate internal representations of continuous variables with a handful of neurons. *Nat. Neurosci.* 27, 2207–2217 (2024).
- Wilson, H. R. & Cowan, J. D. A mathematical theory of the functional dynamics of cortical and thalamic nervous tissue. *Kybernetik* 13, 55–80 (1973).
- Ermentrout, G. B. & Cowan, J. D. A mathematical theory of visual hallucination patterns. *Biol. Cybern.* 34, 137–150 (1979).
- 43. Miller, P. Dynamical systems, attractors, and neural circuits. *F1000Research* **5**, 992 (2016).
- 44. Samsonovich, A. & McNaughton, B. L. Path integration and cognitive mapping in a continuous attractor neural network model. *J. Neurosci.* **17**, 5900–5920 (1997).
- 45. Ocko, S. A., Hardcastle, K., Giocomo, L. M. & Ganguli, S. Emergent elasticity in the neural code for space. *Proc. Natl Acad. Sci.* **115**, E11798–E11806 (2018).
- Fung, C. A., Wong, K. M. & Wu, S. A moving bump in a continuous manifold: a comprehensive study of the tracking dynamics of continuous attractor neural networks. *Neural Comput.* 22, 752–792 (2010).
- Salinas, E. & Abbott, L. F. A model of multiplicative neural responses in parietal cortex. Proc. Natl Acad. Sci. 93, 11956–11961 (1996).
- 48. Solstad, T., Moser, E. I. & Einevoll, G. T. From grid cells to place cells: a mathematical model. *Hippocampus* **16**, 1026–1031 (2006).
- 49. Yan, Y., Burgess, N. & Bicanski, A. A model of head direction and landmark coding in complex environments. *PLoS Comput. Biol.* **17**, e1009434 (2021).
- Lyu, C., Abbott, L. & Maimon, G. Building an allocentric travelling direction signal via vector computation. *Nature* 601, 92–97 (2022).
- McNaughton, B., Chen, L. & Markus, E. Dead reckoning, landmark learning, and the sense of direction: a neurophysiological and computational hypothesis. J. Cogn. Neurosci. 3, 190–202 (1991).
- McNaughton, B. L., Knierim, J. J. & Wilson, M. A. Vector Encoding and the Vestibular Foundations of Spatial Cognition: Neurophysiological and Computational Mechanisms, 585–595 (The MIT Press, 2020).
- Dayan, P. & Abbott, L. F.Theoretical Neuroscience: Computational and Mathematical Modeling of Neural Systems (The MIT Press, 2005).
- 54. Seung, H. S., Lee, D. D., Reis, B. Y. & Tank, D. W. The autapse: a simple illustration of short-term analog memory storage by tuned synaptic feedback. *J. Comput. Neurosci.* **9**, 171–185 (2000).
- Seung, H. S., Lee, D. D., Reis, B. Y. & Tank, D. W. Stability of the memory of eye position in a recurrent network of conductancebased model neurons. *Neuron* 26, 259–271 (2000).
- Taube, J. S. & Burton, H. L. Head direction cell activity monitored in a novel environment and during a cue conflict situation. *J. Neuro*physiol. **74**, 1953–1971 (1995).
- 57. Knight, R. et al. Weighted cue integration in the rodent head direction system. *Philos. Trans. R. Soc. B Biol. Sci.* **369**, 20120512 (2014).
- Zugaro, M. B., Tabuchi, E. & Wiener, S. I. Influence of conflicting visual, inertial and substratal cues on head direction cell activity. *Exp. Brain Res.* 133, 198–208 (2000).
- Wittlinger, M., Wehner, R. & Wolf, H. The ant odometer: stepping on stilts and stumps. Science 312, 1965–1967 (2006).

- Proffitt, D. R., Stefanucci, J., Banton, T. & Epstein, W. The role of effort in perceiving distance. *Psychol. Sci.* 14, 106–112 (2003).
- 61. Lhuillier, S., Gyselinck, V., Dutriaux, L., Grison, E. & Nicolas, S. "like a ball and chain": altering locomotion effort perception distorts spatial representations. *J. Environ. Psychol.* **60**, 63–71 (2018).
- 62. Ko, G. Y.-P., Shi, L. & Ko, M. L. Circadian regulation of ion channels and their functions. *J. Neurochem.* **110**, 1150–1169 (2009).
- 63. Naseri Kouzehgarani, G., Bothwell, M. Y. & Gillette, M. U. Circadian rhythm of redox state regulates membrane excitability in hippocampal ca1 neurons. *Eur. J. Neurosci.* **51**, 34–46 (2020).
- Rieser, J. J., Pick, H. L., Ashmead, D. H. & Garing, A. E. Calibration of human locomotion and models of perceptual-motor organization. J. Exp. Psychol. Hum. Percept. Perform. 21, 480 (1995).
- Low, I. I., Williams, A. H., Campbell, M. G., Linderman, S. W. & Giocomo, L. M. Dynamic and reversible remapping of network representations in an unchanging environment. *Neuron* 109, 2967–2980 (2021).
- Wu, S., Hamaguchi, K. & Amari, S.-i Dynamics and computation of continuous attractors. *Neural Comput.* 20, 994–1025 (2008).
- 67. Wilson, R. C. & Finkel, L. H. A neural implementation of the Kalman filter. *Adv. Neural Inf. Process. Syst.* **22**, 2728–2736 (2009).
- Kutschireiter, A., Basnak, M. A., Wilson, R. I. & Drugowitsch, J. Bayesian inference in ring attractor networks. *Proc. Natl Acad. Sci.* 120, e2210622120 (2023).
- Pouget, A., Zhang, K., Deneve, S. & Latham, P. E. Statistically efficient estimation using population coding. *Neural Comput.* 10, 373–401 (1998).
- Zhang, W.-H., Chen, A., Rasch, M. J. & Wu, S. Decentralized multisensory information integration in neural systems. *J. Neurosci.* 36, 532–547 (2016).
- Åström, K. J. & Wittenmark, B. Adaptive Control (Courier Corporation, 2013).
- Schultz, W. Predictive reward signal of dopamine neurons. J. Neurophysiol. 80, 1–27 (1998).
- Hollerman, J. R. & Schultz, W. Dopamine neurons report an error in the temporal prediction of reward during learning. *Nat. Neurosci.* 1, 304–309 (1998).
- Medina, J. F. & Lisberger, S. G. Links from complex spikes to local plasticity and motor learning in the cerebellum of awake-behaving monkeys. *Nat. Neurosci.* 11, 1185–1192 (2008).
- Kitazawa, S., Kimura, T. & Yin, P.-B. Cerebellar complex spikes encode both destinations and errors in arm movements. *Nature* 392, 494–497 (1998).
- Wang, C.-H., Monaco, J. D. & Knierim, J. J. Hippocampal place cells encode local surface-texture boundaries. *Curr. Biol.* 30, 1397–1409 (2020).
- Ginosar, G., Aljadeff, J., Las, L., Derdikman, D. & Ulanovsky, N. Are grid cells used for navigation? on local metrics, subjective spaces, and black holes. *Neuron* 111, 1858–1875 (2023).
- Hollup, S. A., Molden, S., Donnett, J. G., Moser, M.-B. & Moser, E. I. Accumulation of hippocampal place fields at the goal location in an annular watermaze task. J. Neurosci. 21, 1635–1644 (2001).
- 79. Bourboulou, R. et al. Dynamic control of hippocampal spatial coding resolution by local visual cues. *eLife* **8**, e44487 (2019).
- Krupic, J., Bauza, M., Burton, S., Barry, C. & O'Keefe, J. Grid cell symmetry is shaped by environmental geometry. *Nature* 518, 232–235 (2015).
- 81. Stensola, H. et al. The entorhinal grid map is discretized. *Nature* **492**, 72–78 (2012).
- Barry, C., Hayman, R., Burgess, N. & Jeffery, K. J. Experiencedependent rescaling of entorhinal grids. *Nat. Neurosci.* 10, 682–684 (2007).
- Barry, C., Ginzberg, L. L., O'Keefe, J. & Burgess, N. Grid cell firing patterns signal environmental novelty by expansion. *Proc. Natl Acad. Sci.* 109, 17687–17692 (2012).

- 84. Keinath, A. T., Epstein, R. A. & Balasubramanian, V. Environmental deformations dynamically shift the grid cell spatial metric. *eLife* **7**, e38169 (2018).
- 85. Hetherington, P. A. & Shapiro, M. L. Hippocampal place fields are altered by the removal of single visual cues in a distance-dependent manner. *Behav. Neurosci.* **111**, 20 (1997).
- 86. Eichenbaum, H., Wiener, S. I., Shapiro, M. & Cohen, N. The organization of spatial coding in the hippocampus: a study of neural ensemble activity. *J. Neurosci.* **9**, 2764–2775 (1989).
- Sato, M. et al. Distinct mechanisms of over-representation of landmarks and rewards in the hippocampus. *Cell Rep.* 32, 107864 (2020).
- 88. Cheadle, S. et al. Adaptive gain control during human perceptual choice. *Neuron* **81**, 1429–1441 (2014).
- 89. Keung, W., Hagen, T. A. & Wilson, R. C. A divisive model of evidence accumulation explains uneven weighting of evidence over time. *Nat. Commun.* **11**, 2160 (2020).
- Brunton, B. W., Botvinick, M. M. & Brody, C. D. Rats and humans can optimally accumulate evidence for decision-making. *Science* 340, 95–98 (2013).
- 91. Gallistel, C. R. Animal cognition: the representation of space, time and number. *Ann. Rev. Psychol.* **40**, 155–189 (1989).
- Collett, T. S. & Graham, P. Animal navigation: path integration, visual landmarks and cognitive maps. *Curr. Biol.* 14, R475–R477 (2004).
- 93. Goodridge, J. P. & Touretzky, D. S. Modeling attractor deformation in the rodent head-direction system. *J. Neurophysiol.* **83**, 3402–3410 (2000).
- 94. Madhav, M. S. et al. Control and recalibration of path integration in place cells using optic flow. *Nat. Neurosci.* **27**, 1599–1608 (2024).

## **Acknowledgements**

This work was supported by Johns Hopkins Kavli Discovery Institute postdoctoral fellowship (G.S.) and by National Institutes of Health grants R01 NS102537 (N.J.C., J.J.K.), U01 NS131438 (N.J.C.), and R01 MH118926 (J.J.K., N.J.C.). We thank Ravikrishnan Jayakumar, Kathryn Hedrick, Bharath Krishnan, Manu Madhav, Francesco Savelli, and Kechen Zhang for their helpful comments during the development of this work.

# **Author contributions**

G.S., J.J.K., and N.J.C. conceptualized the study. G.S. and N.J.C. performed the theoretical and computational analyses. J.J.K. provided critical feedback. G.S., J.J.K., and N.J.C. wrote the paper.

# **Competing interests**

The authors declare no competing interests.

### **Additional information**

**Supplementary information** The online version contains supplementary material available at https://doi.org/10.1038/s41467-025-63817-0.

**Correspondence** and requests for materials should be addressed to Gorkem Secer or Noah J. Cowan.

**Peer review information** *Nature Communications* thanks the anonymous reviewer(s) for their contribution to the peer review of this work. A peer review file is available.

**Reprints and permissions information** is available at http://www.nature.com/reprints

**Publisher's note** Springer Nature remains neutral with regard to jurisdictional claims in published maps and institutional affiliations.

Open Access This article is licensed under a Creative Commons Attribution-NonCommercial-NoDerivatives 4.0 International License, which permits any non-commercial use, sharing, distribution and reproduction in any medium or format, as long as you give appropriate credit to the original author(s) and the source, provide a link to the Creative Commons licence, and indicate if you modified the licensed material. You do not have permission under this licence to share adapted material derived from this article or parts of it. The images or other third party material in this article are included in the article's Creative Commons licence, unless indicated otherwise in a credit line to the material. If material is not included in the article's Creative Commons licence and your intended use is not permitted by statutory regulation or exceeds the permitted use, you will need to obtain permission directly from the copyright holder. To view a copy of this licence, visit <a href="https://creativecommons.org/licenses/by-nc-nd/4.0/">https://creativecommons.org/licenses/by-nc-nd/4.0/</a>.

© The Author(s) 2025